JOURNAL OF GEOPHYSICAL RESEARCH, VOL. 101, NO. D3, PAGES 7049–7073, MARCH 20, 1996

Response of a stably stratified atmosphere to large-scale diabatic forcing with applications to wind patters in Brazil and the Sahel

T.-A. Wang, Y.-L. Lin, H. F. M. Semazzi,[1] and G. S. Janowitz

Department of Marine, Earth, and Atmospheric Sciences, North Carolina State University, Raleigh

Abstract. The response of a stably stratified atmospheric flow to large-scale elevated and low-level thermal forcing on a β plane at several latitudes are investigated using a simple nonlinear numerical model. The formation of a westerly jet at the equator, a pair of low-pressure and cyclonic circulation regions, and the decoupling of the westerly jet and the heating center are explained by the β effect. It is found that the vertical motion in the case with heating centered at the equator is much larger than that with heating centered at higher latitudes. This is explained by the trapping of more wave energy in equatorial regions when the heating is centered at the equator. On the other hand, the pressure perturbation is much stronger for cases with heating located at a higher latitude due to vortex stretching. It is found that there exists a vertical phase tilt which is explained by the upward propagating Kelvin waves near the equator and mixed Rossby gravity waves at higher latitudes. The vertical wavelength of the disturbance increases as the heating center is located at a higher latitude. In addition, we find that this type of flow is not sensitive to the existence of the stratosphere. One interesting feature is that the maximum vertical velocity for the case with heating centered at the equator is significantly larger than that with heating centered at 30°N. Comparing both linear and nonlinear cases with surface heating or cooling, we find (1) the nonlinearity suppresses (enhances) the disturbance induced by cooling (heating), (2) the differences between the nonlinear and linear responses are larger when the forcing is located at lower latitudes, and (3) the disturbed areas are much wider in the zonal direction for cooling cases than for cases with heating. The nonlinear effects are studied by inspecting individual terms. To explore the relationships between Atlantic sea surface temperature anomaly (SSTA) and rainfall anomalies in the Sahel and northeastern Brazil, the SSTA is represented by low-level diabatic forcing in the numerical model. With a coupled warm SSTA in the South Atlantic and cold SSTA in the North Atlantic, model results indicate a combination of offshore flow and downward motion in the Sahel, while there exists an upward motion and an offshore flow in northeastern Brazil. When the SSTA pattern is reversed, then there exists an onshore flow and an upward motion in the western Sahel, while there exists a strong onshore flow and a downward motion in northeastern Brazil.

1. Introduction

The influence of the sea surface temperature anomaly (SSTA) on the general circulation has been studied extensively over the past three decades. *Bjerknes* [1966] found some evidence for the effects of SSTA on climate, which was demonstrated numerically by *Rowntree* [1972]. In particular, it has been proposed that the rainfall anomaly over the African Sahel and northeastern Brazil are strongly influenced by the Atlantic ocean SSTA distributions [e.g., *Markham and McLain*, 1977; *Lamb*, 1978; *Moura and Shukla*, 1981; *Hastenrath*, 1984; *Lough*, 1986; *Semazzi et al.*, 1988]. The Sahelian region may be defined as the region between 10°N and 20°N in Africa [*Nicholson*, 1985]. Since SSTA patterns often persist for at least a period of several months [*Moura and Shukla*, 1981], they may have significant impact on the general circulation, and therefore, on the long-term weather and climate. One example is the Sahelian rainfall anomalies and their relationship with the Atlantic SSTAs in the period of 1967 to 1968 (Figure 1). Notice that the positive rainfall anomaly in 1967 was strongly correlated to the couplet of warm and cold SSTA in northern and southern Atlantic oceans, respectively, while the rainfall anomaly and the SSTA couplet were both reversed in 1968. Most of the precipitation in African Sahel occurs between July and September. The southwesterly wind from southeast Atlantic provides the moisture, low-level convergence and upward motion which are all responsible for producing the rainfall during this period (Figure 2). Therefore understanding the role of SSTA on wind patterns is important since the wind patterns may affect the rainfall distributions in the adjacent continents.

In northern and central regions of northeastern Brazil, the seasonal distribution of rainfall shows a sharp peak in March-April, when the intertropical convergence zone (ITCZ) is in its extreme southern position; the southern region receives its maximum precipitation from November to March with a peak in December [*Ratisbona*, 1976]. *Moura and Shukla* [1981] investigated the mechanism for the occurrence of droughts over northeastern Brazil by incorporating observed SSTA distributions in a general circulation model (GCM). Observations [e.g., *Hastenrath and Heller*, 1977; *Hastenrath*, 1978] show that in years of droughts, SSTA in the tropical Atlantic displays a pattern of positive values to the north and

[1]Also at Department of Mathematics, North Carolina State University, Raleigh.

Paper number 95JD03761.
0148-0227/96/95JD-03761$05.00

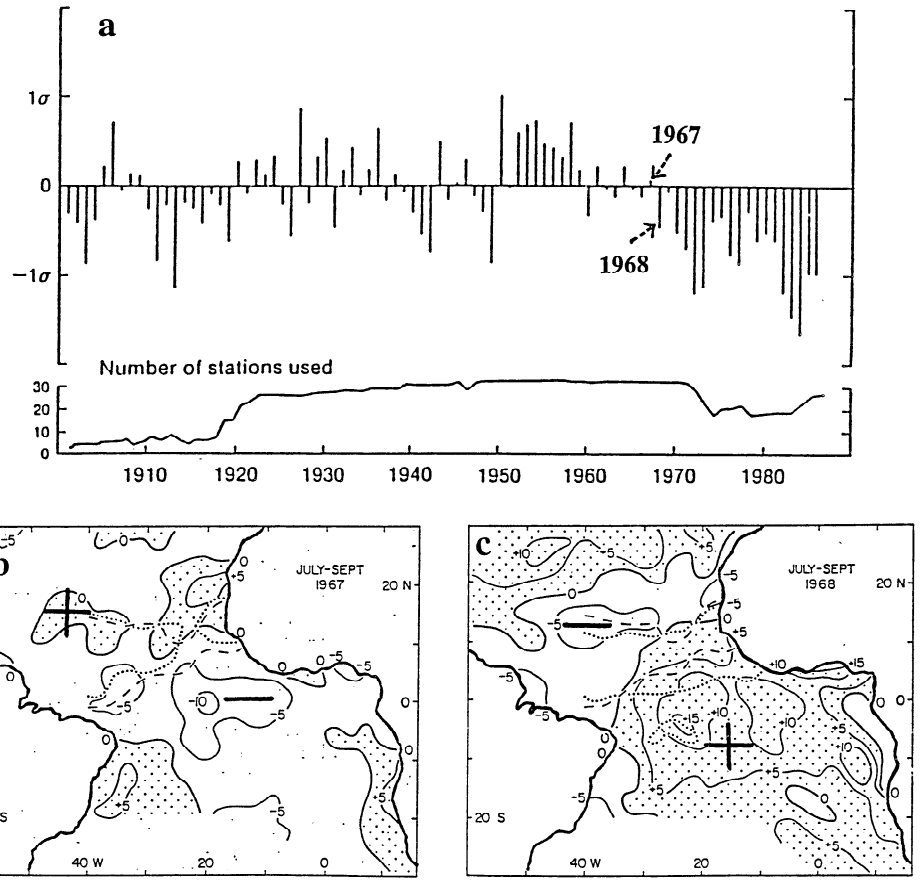

Figure 1. (a) Standardized annual rainfall anomalies for the Sahel, 1901-1986 [after *Parker et. al. [1988]* (b) SST fields for July-September 1967, and (c) same as Figure 1b except for 1968 [After *Lamb*, 1978].

negative values to the south of equator. For wet years the pattern is essentially reversed. Using a prescribed heating in an analytical model, they suggested that there is an ascending (descending) motion, low-level cyclonic (anticyclonic) circulation, and upper level anticyclonic (cyclonic) circulations collocated with the warm (cold) SSTA. Comparing the analytical results to those from GCMs, they found that the results are surprisingly consistent, indicating that the major features of the response can be understood in terms of linear dynamics. They suggested that the low-level anticyclonic vorticity and high pressure located to the south of equator provides low-level divergence of moisture flux which is responsible for the observed decrease in rainfall over northeast Brazil. However, they used an elevated heating and cooling to the north and south of the equator, respectively, to represent the diabatic forcing associated with SSTA in their study. Although prescribed elevated heating may, as a first approximation, represent the latent heat release associated with deep convection, it is physically questionable to adopt an elevated cooling.

Many investigators have utilized GCMs to simulate the influence of SSTA on the general circulation and the occurrence of droughts [e.g., *Spar*, 1973; *Houghton et al.*, 1974; *Moura and Shukla*, 1981; *Shukla and Wallace*, 1983; *Palmer and Mansfield*, 1986]. The advantage of using GCMs is that it is relatively easy to simulate the response by directly incorporating observational SSTA data into the model. However, *Egger* [1977] argued that GCMs usually have the problem of signal-to-noise ratio. Although it is possible to resolve this problem [*Chervin and Schneider*, 1976], it is still very difficult to gain insight into the physical processes which link the SSTA distribution and the simulated rainfall anomalies due to the underlying complexity of the GCM itself. In addition, *Schneider and Lindzen* [1977] and *Stevens and Lindzen* [1978] suggested that the flows generated by cumulus heating do not respond effectively to low-level convergence, at least for timescales greater than 1 week. *Lindzen and Nigam* [1987] adopted a simple one-layer (surface to 700 mbar) model to study the effects of SST gradients on low-level flow and convergence in the tropics over timescales greater or equal to 1 month. The results suggested that the flows directly induced by surface temperature are similar to the observational low-level flows in both magnitude and morphology. This type of investigation can be improved by using a continuously stratified numerical model such as that used in the present study.

There have been several theoretical studies concerned with the large-scale heat-induced motions in the tropics [e.g., *Matsuno*, 1966; *Webster*, 1972; *Gill*, 1980; *Phlips and Gill*, 1987]. Using a divergent barotropic model, *Matsuno* [1966] found that both inertia gravity waves and Rossby waves are forced by diabatic heating in the equatorial area. Using a linear theory, *Gill* [1980] found that both Kelvin waves and Rossby waves exist in the atmospheric response to a prescribed heating in the tropics, which propagate toward east and west, respectively. *Gill and Phlips* [1986] compared both the linear and nonlinear solutions for the atmospheric response to an isolated region of heating centered at the equator using an analytical model. They concluded that nonlinear effects are important dynamically, but the departures from linear theory are more in the way of a modest distortion of the flow field than any qualitative change in

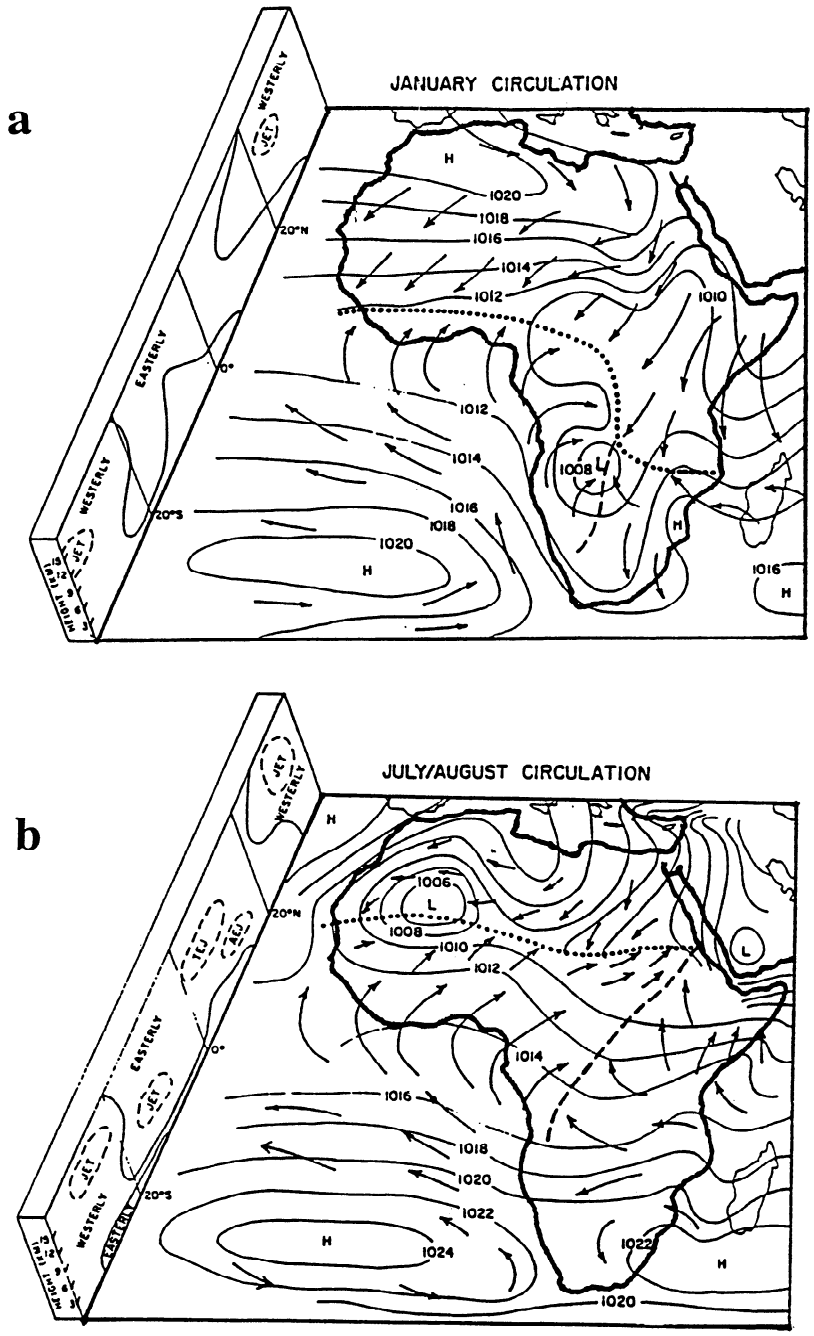

Figure 2. Atmospheric circulation (winds and pressure) over Africa for (a) January and (b) July-August, including schematic of winds aloft, jet streams, and surface convergence zones [after *Nicholson et al.*, 1988].

behavior. The nonlinear effects are significant only near the western end of the heating region and in the decay region immediately to the west of the thermal forcing. *Phlips and Gill* [1987] used a linear analytical model to extend the work of Gill by including a basic wind and investigated the effects of different heating geometries and values of Rayleigh friction. This type of approach in using a prescribed heating has also been found very useful in understanding mesoscale circulations (*Lin and Stewart* [1991] and *Lin* [1994a,b]).

In this study we will use a simple nonlinear numerical model to investigate the large-scale response of the tropical and subtropical atmosphere to both prescribed elevated and low-level diabatic forcing. The numerical results will be compared to those with other studies [e.g., *Gill*, 1980; *Phlips and Gill*, 1987]. The structure of this paper is as follows. The numerical model will be described in section 2. The response of the atmosphere to elevated heating will be discussed in section 3, while the response to low-level surface heating will be discussed in section 4. In section 5, the influence of SSTA on wind patterns in the African Sahel and northeastern Brazil will be investigated by prescribing either a single or a couplet of heat source/sink in the numerical model. Concluding remarks are made in the last section.

2. The Model

The equations governing thermally forced finite amplitude perturbations in a continuously stratified Boussinesq atmosphere on a β plane may be written as:

$$\frac{\partial u}{\partial t}+(U+u)\frac{\partial u}{\partial x}+(V+v)\frac{\partial u}{\partial y}+w\left(\frac{\partial U}{\partial z}+\frac{\partial u}{\partial z}\right)$$

$$-\left[f_o+\beta(y-y_o)\right]v=-\frac{\partial \phi}{\partial x}-\varepsilon u, \tag{1}$$

$$\frac{\partial v}{\partial t}+(U+u)\frac{\partial v}{\partial x}+(V+v)\frac{\partial v}{\partial y}+w\left(\frac{\partial V}{\partial z}+\frac{\partial v}{\partial z}\right)$$

$$+\left[f_o+\beta(y-y_o)\right]u=-\frac{\partial \phi}{\partial y}-\varepsilon v, \tag{2}$$

$$\frac{\partial \theta}{\partial t}+(U+u)\frac{\partial \theta}{\partial x}+(V+v)\frac{\partial \theta}{\partial y}+\left(u\frac{\partial \Theta}{\partial x}+v\frac{\partial \Theta}{\partial y}\right)$$

$$+w\left(\frac{\partial \theta}{\partial z}+\frac{N^2\theta_o}{g}\right)=\frac{\theta_o}{c_pT_o}Q-\varepsilon\theta \tag{3}$$

$$\frac{\partial u}{\partial x}+\frac{\partial v}{\partial y}+\frac{\partial w}{\partial z}=0, \tag{4}$$

$$\frac{\partial \phi}{\partial z}=g\frac{\theta}{\theta_o} \tag{5}$$

where

- u perturbation horizontal velocity in x direction;
- v perturbation horizontal velocity in y direction;
- w perturbation vertical wind velocity;
- θ perturbation potential temperature;
- ϕ perturbation kinematic pressure (p/ρ_0);
- U basic wind velocity in x direction;
- V basic wind velocity in y direction;
- Θ basic potential temperature;
- ρ_o constant reference density;
- T_o constant reference temperature;
- θ_o constant reference potential temperature;
- N Brunt-Vaisala frequency;
- f_o Coriolis parameter at a certain latitude;
- β variation of Coriolis parameter with latitude;
- y_o location of the heating center;
- ε Rayleigh friction and Newtonian cooling coefficient;
- Q diabatic heating rate per unit mass (Joules per kilogram per second);
- c_p specific heat capacity of dry air at constant pressure; and
- g gravitational acceleration.

Notice that the replacement of the continuity equation by the incompressible form under the Boussinesq of approximation does not imply that the density is regarded as constant following the motion, but simply that the magnitude of $\rho^{-1}(D\rho/Dt)$ is small in comparison to the magnitudes of the velocity gradients [e.g., *Kundu*, 1990]. The Brunt-Vaisala frequency is assumed to be independent of height throughout this study. In this model the wind components in x and y directions and the potential temperature are separated into basic (U, V, Θ) and perturbation parts (u', v', θ'), for convenience in isolating the nonlinear effects. The basic state wind fields are assumed to be functions of the vertical coordinate only, that is, no horizontal shear of the basic state flow is considered in this model. The horizontal and vertical derivatives are approximated by a fourth-order and second-order centered finite difference schemes, respectively. The temporal derivatives are approximated by the leapfrog scheme, with the exception of the first time step, which is computed by forward finite differencing. Viscous effects are modeled through the inclusion of Rayleigh friction and Newtonian cooling terms in the horizontal momentum and thermodynamic energy equations, respectively.

For flow over a flat surface, such as the cases considered in this study, the lower boundary condition is simply that w= 0. For the upper boundary condition, the model adopts the radiation condition [*Klemp and Durran*, 1983] in order to allow the wave energy to propagate out of the domain. A radiation lateral boundary condition is employed [*Orlanski*, 1976]. A five-point numerical smoothing [Shapiro, 1970] in space is employed in both the horizontal and vertical directions, while a three-point numerical smoothing in time is adopted [Asselin, 1972]. Both the horizontal and vertical smoothing coefficients are taken to be 1/128. However, this smoother is able to suppress the $2\Delta x$ waves effectively, even though it is very weak. The details of the numerical model may be found in work by *Lin et al.* [1993] and *Weglarz* [1994]. The present numerical results have been tested against theoretical solutions of *Gill* [1980] and *Phlips and Gill* [1987] for flow over a large-scale heat source on a β plane, which compare very well with their theoretical counterparts (Figure 3).

3. Response to Elevated Heating

The time independent heating function is specified as follows

$$Q(x,y,z)=Q_o\cos\left(\frac{\pi x}{2L_x}\right)\exp\left[-\left(\frac{y-y_o}{2L_y}\right)^2\right]$$

$$\sin\left[\frac{\pi z}{Z_T-Z_b}\right],\ \text{for } |x|\le L_x \text{ and } z_b\le z\le z_T, \tag{6a}$$

$$Q(x,y,z)=0, \qquad \text{elsewhere.} \tag{6b}$$

In order to make direct comparisons with *Gill* [1980] and *Phlips and Gill* [1987], we have adopted the same heating function which is able to represent the isolated region of Atlantic SSTA (Figure 1b-1c). The heating parameters used in these simulations are Q_o=0.03 J kg^{-1}s^{-1}, L_x=2000 km, L_y=1000 km, z_b=0 km, and z_T=10 km. The heating rate is comparable to that of *Gill* [1980]. The heating rate associated with the elevated latent heating is related to the rainfall rate according to the following equation [e.g., see *Smith and Lin*, 1982]

$$\rho_o\int_0^\infty Q_oH(z)dz=R\rho_w\lambda \tag{7}$$

where $H(z)$ is the normalized vertical distribution of the latent heating, R the maximum rainfall rate, ρ_W the liquid water density (10^3 kg m^{-3}), λ the latent heating of condensation (2.5×10^6 J kg^{-1}), and ρ_o the air density. With the vertical distribution of heating specified in (6), we have

$$R=\frac{2\rho_o(z_T-z_b)}{\pi\rho_w\lambda}Q_o \tag{8}$$

The rainfall rate corresponding to Q_O=0.03 J kg^{-1} s^{-1} is 0.3 mm h^{-1}. Other flow parameters are U=0 ms^{-1}, N=0.01 s^{-1}, $\varepsilon=2.28\times10^{-6}$ s^{-1}, c_p=1004 J K^{-1}kg^{-1}, R=287.05 J K^{-1}kg^{-1}, and g=9.80665 ms^{-2}. The numerical parameters of the model used in this section are Δt=360 s, Δx=500 km, Δy=250 km, and Δz=500 m. The number of grid points is 32x32x41. The total simulation time is 16-days for all cases presented in this section. After 16-day simulation, the results can be considered to be quasi-steady state as will be shown from the time evolution of pressure perturbation and vertical velocity fields later (Figure 4e and 4f).

Figure 3 shows the horizontal vector wind, vertical velocity, and perturbation pressure fields at z=500 m for a quiescent

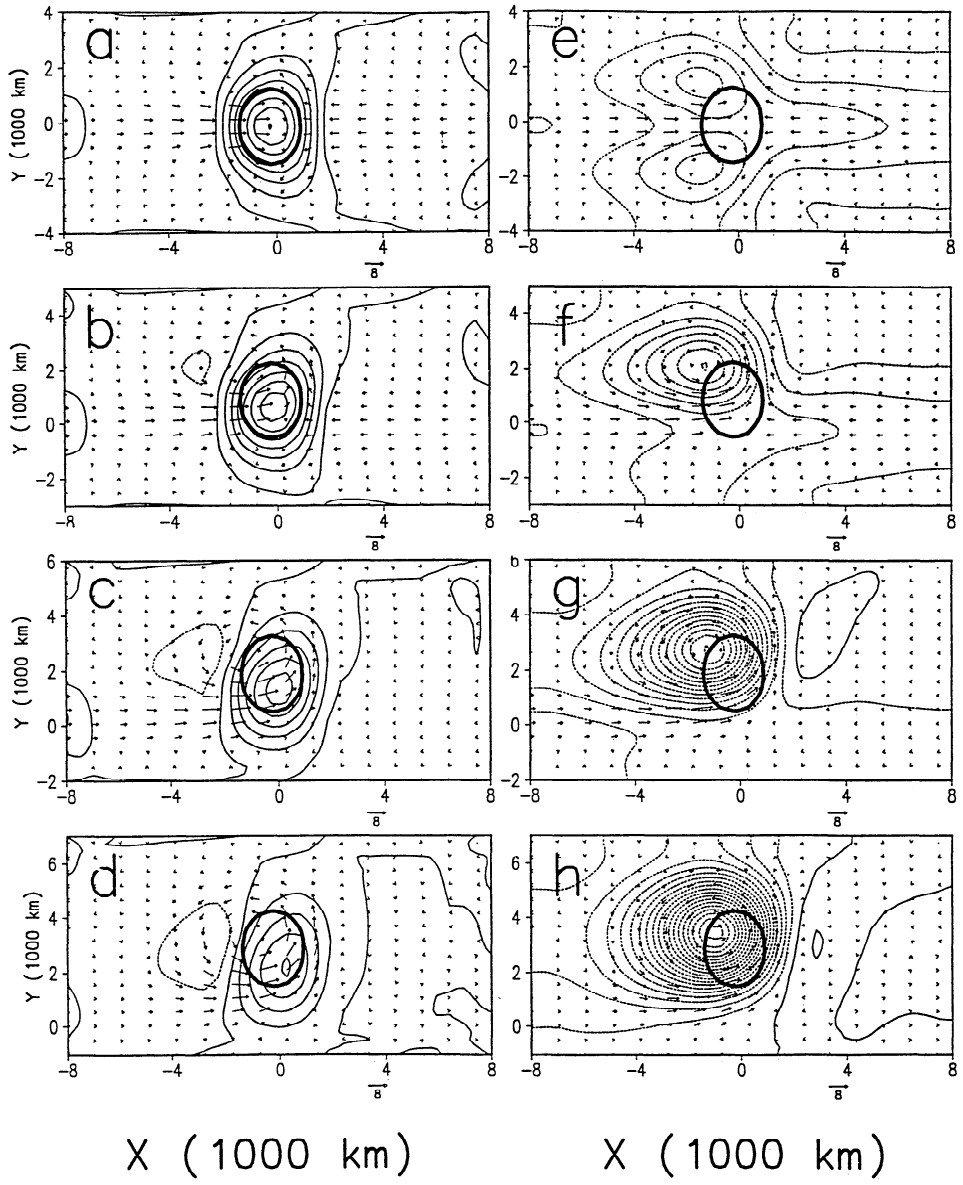

Figure 3. The horizontal perturbation vector wind, vertical velocity (thin contour lines on left panels, in meters per second), and the perturbation pressure (thin contour lines on right panels, in pascal) at z=500 m for an elevated heating, which is specified by (6), (a, e) centered at the equator, (b, f) 10°N, (c, g) 20°N, (d, h) 30°N after 16 days. The heating is concentrated in the region enclosed by the thick solid line. The contour intervals of w and p in Figures 3a-3h are 0.0002 ms^{-1} and 50 Pa, respectively. The scale of the horizontal wind vectors is denoted in the figure (in meters per second).

atmosphere (U, V=0) with heating centered at different latitudes after 16 d. In the case when the heating centered at the equator, the disturbance is symmetric with respect to the equator since both the forcing and rotational effects are symmetric about the equator in this case (Figures 3a and 3e). A pair of low-pressure regions form to the north and south of the equator (Figure 3e). This result is similar to that of *Gill* [1980]. A westerly jet forms on the western side of the heating center. Near the equator, the westerly jet on the western side of the heat source is stronger than the easterly wind on the eastern side of the heat source. A couplet of cyclonic circulations forms to the northwest and southwest of the heating center (Figure 3a). In Figure 3a, there exists an upward motion in the heating region and the maximum vertical velocity occurs at the heating center.

The formation of the westerly jet at the equator, low-pressure regions and cyclonic circulations induced by the heating may be understood by investigating the transient response (Figure 4). At an early stage of the response, the heating produces a pool of warm air, which is then able to produce an upward motion, in the vicinity of the heat source, as required by the thermodynamic equation. Through the hydrostatic balance, this in turn generates a low pressure around the heat source (Figure 4a). The pressure gradient force associated with the low pressure produces convergence of airflow toward the heating center. The vertical motion produced by these processes is constrained by the mass continuity equation. This explains why the maximum upward velocity exists in the vicinity of the heat source at later times (Figure 3a). During the adjustment stage (Figures 4b-4d), the flow convergence near the equator is not influenced by rotation since the Coriolis force is very weak there. Away from the equator, the thermally induced flow deflects toward right (left) in the northern (southern) hemisphere due to the Coriolis force. The deflection increases with the distance from the equator. The convergence in the zonal direction at the equator near the heat

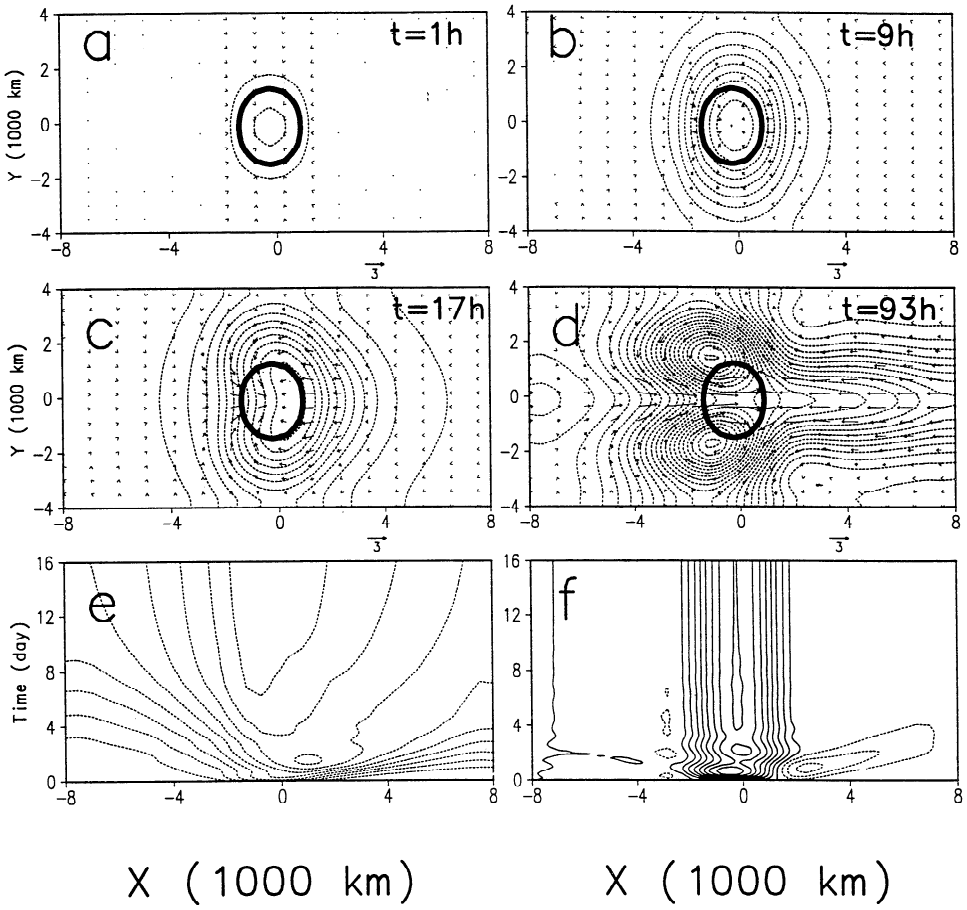

Figure 4. Four time steps: (a) 1 hour, (b) 9 hour, (c) 17 hour, and (d) 93 hour of the horizontal perturbation vector wind and the perturbation pressure at z=500 m for the case of Figure 3e. The contour interval of p is 10 Pa. The corresponding time evolutions of perturbation pressure and vertical velocity fields at y=0 are shown in Figure 4e and 4f, respectively.

center produces poleward flows along the y axis. This poleward flow overcomes the equatorward flow produced in the earlier stage and helps to generate cyclonic circulations which are located to the northwest and southwest of the heating center. Low-pressure perturbations are then produced by the cyclonic circulations which also strengthen the westerly flow near the equator (Figure 3e). The addition of the eastward perturbation winds associated with these two cyclonic circulations finally produces the westerly jet at the equator (Figure 3a).

The vertical velocity and horizontal vector wind fields for the cases with heating centered at 10°N ($y \approx 1000$ km), 20°N ($y \approx 2000$ km), and 30°N ($y \approx 3000$ km) are also shown in Figure 3. In general, an upward motion is produced in the vicinity of the heating region. However, the maxima of vertical velocities are not necessarily located at the heating center except for the case with heating centered at the equator (Figure 3a). When the heat source is located at a higher latitude, the vertical velocity maximum is shifted to the southeast of the heating center, which is collocated with the horizontal velocity maximum. Notice that the center of the cyclonic circulation is closer to the heating center when the heating is located at higher latitudes.

The relative positions of the westerly jet and heating center are different when the heating is located at a different latitudes. The location of the westerly jet is also determined by the β effect. To explain this phenomenon, we may consider the zonal geostrophic flow

$$fu = -\frac{\partial \phi}{\partial y} \tag{9}$$

By considering two points to the north and south of the low-pressure center, which have comparable pressure gradient in y direction (Figures 3f-3h), the above equation indicates that u is larger when f is smaller. Therefore the westerly jet always forms to the south of the heating center when the heating center is located to the north of the equator.

One significant result is that the vertical motion in the case with heating centered at the equator is almost twice as large as when heating is centered at 30°N (Figures 3a and 3d). This can be explained by (1) there is much more cyclonic flow around the heating center at higher latitudes (Figure 3d), which in turn produces less convergence and vertical motion, and (2) the equatorial heating forces mostly Kelvin waves, while the higher latitude heating forces mostly Rossby waves (Figure 3a).

Figure 3e shows the perturbation pressure field. To the north and south of the heat source, the poleward flows near the eastern edge of the heat source and the equatorward flows on the western side of the heat source form closed cyclonic circulations. Two low-pressure centers are associated with these two closed circulations. The poleward flow is forced by the convergence of east-west winds on the eastern side of the heat source. For the wave structures in a case with heating centered at the equator, *Gill* [1980] found that the heat-induced Kelvin waves propagate at three times the speed of the Rossby waves. Similar wave structures are also shown in our (nonlinear) numerical results. A rough estimate of the phase speed for the westward propagating Rossby wave gives a value of 30 ms^{-1}, which is based on the time evolution of pressure perturbation (Figure 4e). It is also estimated that the phase speed of the Kelvin wave is about three

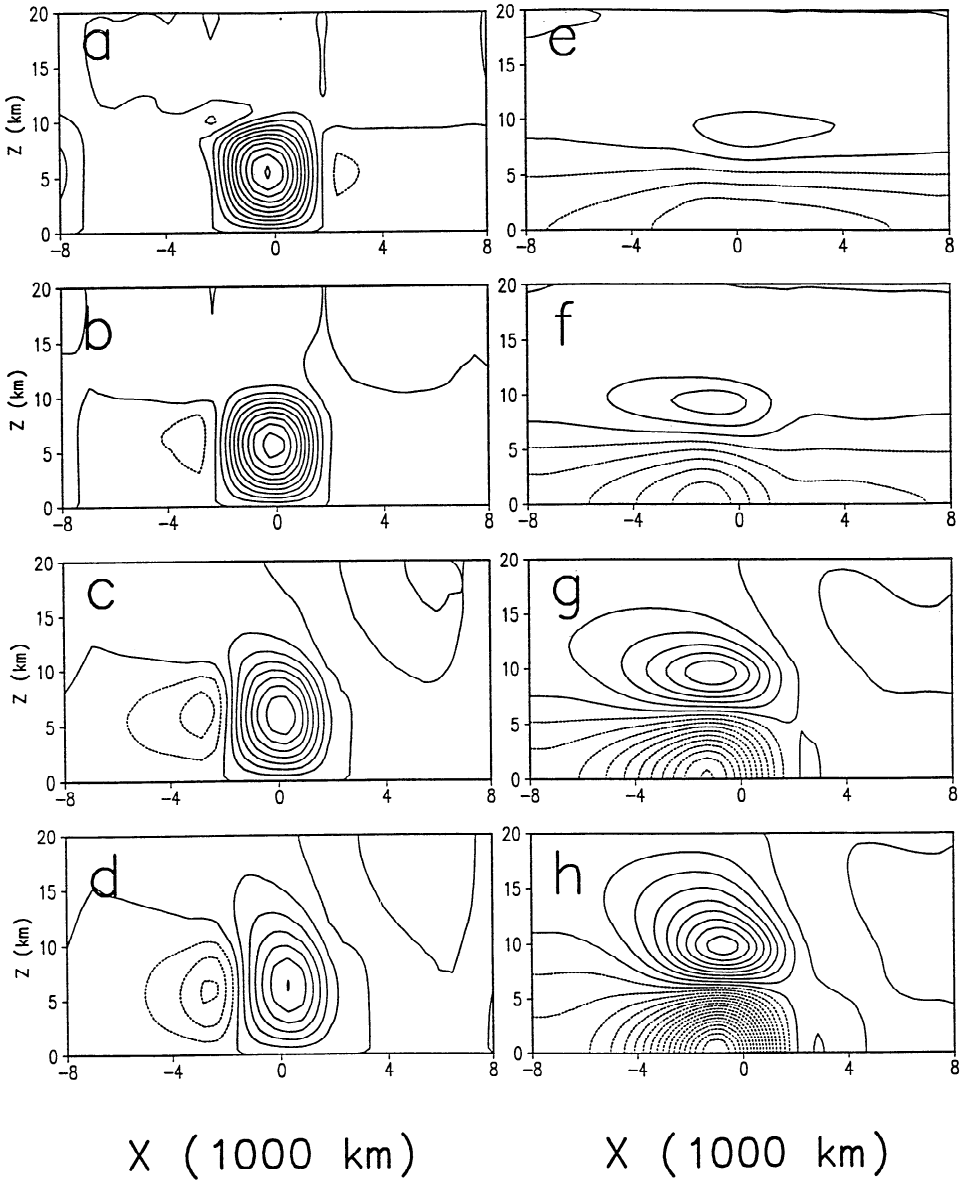

Figure 5. The x-z vertical cross sections of vertical velocity (left panels) and perturbation pressure (right panels) along the latitude of the heating center for cases of Figure 3. The contour intervals of w and p in Figures 5a-5h are 0.001 ms^{-1} and 50 Pa, respectively.

times larger than that of the Rossby wave. Notice that these waves are generated by the β effect (*Matsuno*, 1966). Thus the present result is consistent with A.E. Gill's study. From Figures. 4e and 4f, especially the later, we can also see that the flow approaches a quasi-steady state after 16 days.

The perturbation pressure fields for cases with heating centered at 10°N, 20°N, and 30°N are shown in Figures 3f, 3g, and 3h, respectively. The disturbances are no longer symmetric about the latitude of the heating center since the Coriolis force is not symmetric. When the heating center is located at a higher latitude, the magnitude of the low pressure is significantly strengthened. This increase in absolute values is due to the increase of vortex stretching [*Phlips and Gill*, 1987] which can be seen from the stronger cyclonic circulation. Basically, the pressure fields from the numerical model are consistent with the analytical studies of *Gill* [1980] and *Phlips and Gill* [1987]. In this study the formation of certain features of the heat-induced disturbance, such as the westerly and easterly jets at the equator, cyclonic circulations to the northwest and southwest of the heating center, and the decoupling of the jet and heating center are explained by the β effects. In addition, we find that the vertical motion is much weaker and the pressure perturbation is much stronger for heating located at higher latitudes.

Figure 5 shows the x-z vertical cross sections of vertical velocity and perturbation pressure along the latitude of heating center. For the case with heating centered at the equator (Figure 5a), the structure of the vertical velocity is similar to that of the vertical heating distribution. The maximum upward velocity occurs near the heating maximum, that is, 5 km. At the top boundary, the vertical velocity is almost zero except for the case with heating centered at higher latitude (Figures 5b-5d). This indicates that the rigid lid upper boundary condition used in most of theoretical studies [e.g., *Gill*, 1980] or numerical simulations of large-scale phenomena, is reasonable for this type of problem in lower latitudes. The constant phase of maximum vertical velocity tilts slightly to the east with height for the case with heating centered at the equator (Figure 5a), while it tilts to the west for other cases. This indicates the existence of vertically

propagating waves. The eastward phase tilt may be associated with the eastward propagating Kelvin waves near the equator, while the westward phase tilt may be mostly associated with the Rossby waves. Notice that the heating-induced mixed Rossby gravity wave mode in this type of problem is very small [*Dias et al.*, 1983]. In fact, it is zero for heating centered at equator. Thus the vertically propagating waves may be dominated by Kelvin waves for the case with heating centered at equator.

The vertical tilting, to first approximation, may be explained by quasi-geostrophic dynamics. The linear equation for w with quasi-geostrophic approximation and Rayleigh friction and Newtonian cooling included can be derived,

$$\left(\frac{\partial}{\partial t}+U\frac{\partial}{\partial x}+\varepsilon\right)\left[\nabla_H^2 w+\frac{f_o^2}{N^2}\frac{\partial^2 w}{\partial z^2}\right]+\beta\frac{\partial w}{\partial x}=\frac{1}{N^2}$$

$$\left[\left(\frac{\partial}{\partial t}+U\frac{\partial}{\partial x}+\varepsilon\right)\nabla_H^2+\beta\frac{\partial}{\partial x}\right]\left(\frac{gQ}{c_pT_o}\right). \quad (10)$$

Notice that the gravity wave modes may be ruled out by the quasi-geostrophic approximation due to their relatively short wavelength. However, a certain portion of Kelvin waves with sufficiently long wavelength may still exist. We consider a steady state, wavelike solution of the form,

$$w=\hat{w}(z)\,e^{i(kx+ly)}. \quad (11)$$

Substituting the above equation into (10) with no heating term yields

$$\frac{\partial^2\hat{w}}{\partial z^2}+\lambda^2\hat{w}=0, \quad (12)$$

where

$$\lambda^2=\frac{N^2}{f_0^2}\left[\frac{ik\beta}{ikU+\varepsilon}-\left(k^2+l^2\right)\right]. \quad (13)$$

The solution of (12) is

$$\hat{w}=w_o e^{i\lambda z}. \quad (14)$$

In the above solution, we have applied the upper boundary condition which requires either a radiation condition (first term) or a boundedness condition depending upon whether λ is imaginary or real, respectively. Let $\lambda=\lambda_r+i\lambda_i$ so that

$$e^{i\lambda z}=e^{i(\lambda_r+i\lambda_i)z}=e^{-\lambda_i z}e^{i\lambda_r z} \quad (15)$$

The vertical tilting of the disturbance is due to the $\exp(i\lambda_r z)$ term which allows the wave energy to propagate upward to infinity for shorter waves. An isolated forcing in the x direction generates a wide spectrum of waves. The dominant wavelength is about $4L_x$ (6a). It can be analyzed from (13) that the magnitude of λ_r increases when U decreases and the latitude increases in the range of 0° and 55°. The dependence of λ_r on the variation with latitude and Rayleigh friction coefficient for $U = 0$ is plotted in Figure 6. This explains the vertical tilting of the vertical velocity field as shown in Figures 5a-5d. Figures 5e-5h show that the pressure perturbation is reversed at the level of maximum heating in the vertical, due to mass continuity. The much larger pressure perturbation for cases with heating located at higher latitudes (e.g., Figures 5g-5h) is explained by the vortex stretching as mentioned earlier.

Figure 7 shows the y-z vertical cross sections of vertical velocity and perturbation pressure across the heating center. For

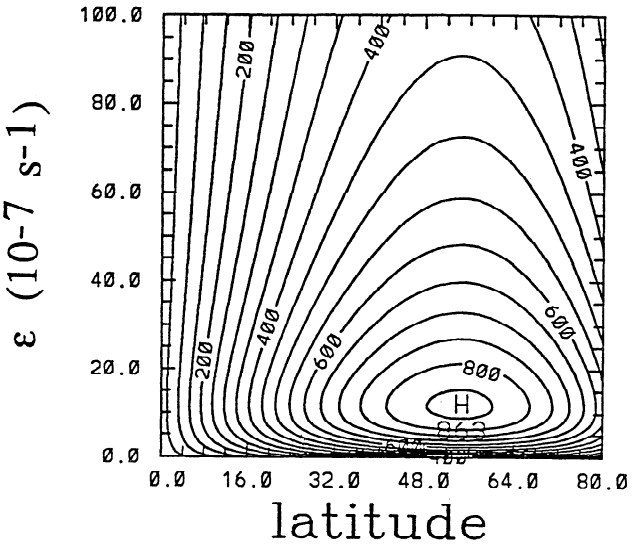

Figure 6. The variation of λ_r to latitude and Rayleigh friction coefficient (ε) for U=0.

heating centered at the equator (Figures 7a and 7e), both the vertical velocity and perturbation pressure fields are symmetric with respect to the x axis at each vertical level. One major feature is the northward phase tilt in the vertical when the heat source is located at higher latitudes, which is caused by the β effect as explained earlier. Two low-pressure cells are located near the surface in the case where heating is centered at the equator (Figure 7e), but notice that the cell located to the south (north) is reduced (enhanced) when the heating is located at a higher latitude (Figures 7f-7h). Owing to mass continuity, there exists a region of divergence at an upper level (z=9.5 km, see Figure 8), although some diabatic heating still exists there. For heating centered at the equator (Figure 8a), it can also be seen that the Kelvin waves propagate at a faster speed than the Rossby waves at this level. The pressure perturbations are positive at this level and they are associated with flow divergence.

Our sensitivity tests on the coefficients of Rayleigh friction and Newtonian cooling and on the basic wind velocities are similar to the findings of *Phlips and Gill* [1987]. In addition, we also find that the effects of stratosphere, that is, the abrupt change of Brunt-Vaisala frequency at tropopause, in this problem is negligible (not shown). Comparing the linear (Figures 9a and 9e) with the nonlinear (Figures 9b and 9f) response for the case of Figure 3a, we find that the nonlinear effects are negligible. However, with a larger heating rate (say, 5 times), the nonlinear effect strengthens the cyclonic circulations and weakens both the westerly and easterly jets near the equator (Figures 9d and 9h) when compared with the linear response (Figures 9c and 9g).

4. Response to Low-Level Heating

In this section, we investigate the influence of surface thermal forcing which is taken to represent the sensible heating or cooling associated with sea surface temperature anomalies (SSTA) in the lower atmosphere. Understanding the atmospheric response to surface heating is important since the low-level heating produces low-level disturbances which precede the onset of moist convection and subsequent latent heat release.

The basic state parameters used in this section are the same as those in section 3 except the vertical function is specified as

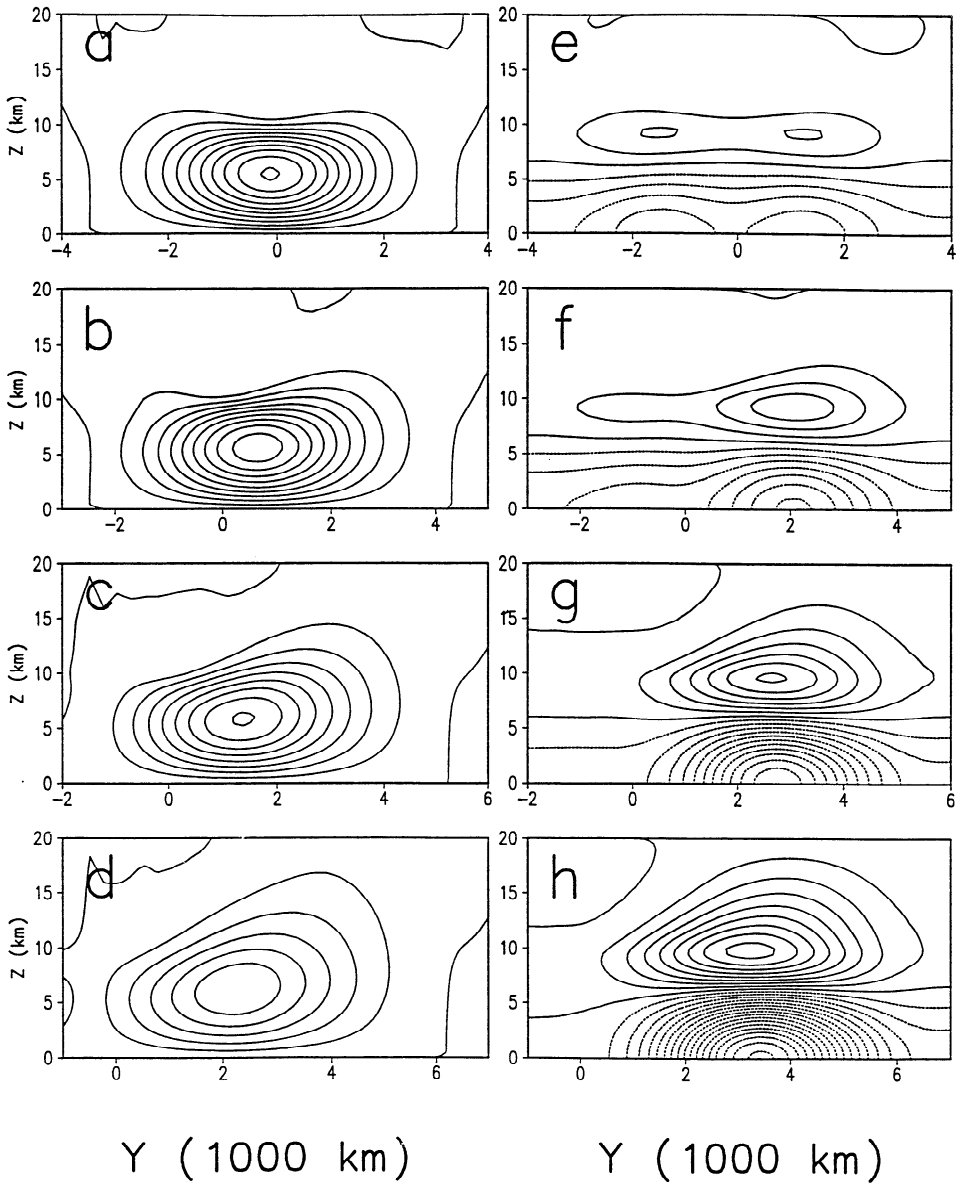

Figure 7. Same as Figure 5 except for the *y-z* vertical cross sections. The contour intervals of w and p in Figure 7a-7h are 0.001 ms^{-1} and 50 Pa, respectively.

$$Q(x,y,z)=Q_o \cos\left(\frac{\pi x}{2L_x}\right)\exp\left[\left(\frac{y-y_o}{2L_y}\right)^2\right]$$

$$\exp\left[\frac{-z}{H_1}\right], \quad \text{for } |x|\le L_x, \tag{16a}$$

$$Q(x,y,z)=0 \qquad \text{elsewhere} \tag{16b}$$

where H_1=1 km is the e folding height of the surface heating and $Q_o=0.016$ J $kg^{-1}s^{-1}$, which corresponds to a heating rate of roughly 1.4 K d^{-1} at the surface. The value of ε is taken to be 1.14×10^{-6} s^{-1}. The corresponding time for the atmosphere to reach a steady state in responding to the heating or cooling is about 15 d. All results presented in this section are for 30-day simulations. A smaller ε is chosen with an e folding time of about 10 days, compared to an e folding time of about 5 days in the previous section. The same values of ε and simulation time will also be used for the effects of SSTA on rainfall anomalies in section 5. This makes it easier to apply the present idealized simulations and compare the results. In order to understand the effects of Atlantic SSTA on the rainfall anomaly in the African Sahel and northeastern Brazil, it is important to investigate the atmospheric response to a low-level sensible heating [*Lindzen and Nigam*, 1987].

Figure 10 shows the horizontal vector wind, vertical velocity and surface perturbation pressure fields at z=500 m induced by an isolated low-level heating centered at the equator, 10°N, 20°N, and 30°N after 30 d. Some aspects of the results are similar to those produced by elevated heating as presented in last section, such as the westerly and easterly jets at the equator, cyclonic circulations to the northwest and southwest of the heating center, and the decoupling of the jet and heating center. One striking feature is that the maximum vertical velocity for the case with heating centered at the equator (Figure 10a) is more than 10 times larger than that with heating centered at 30°N (Figure 10d). The stronger response for the former case has also been observed in the case of elevated heating (Figures 3a and 3d) and explained in the last section. In addition to the reasons which explain the

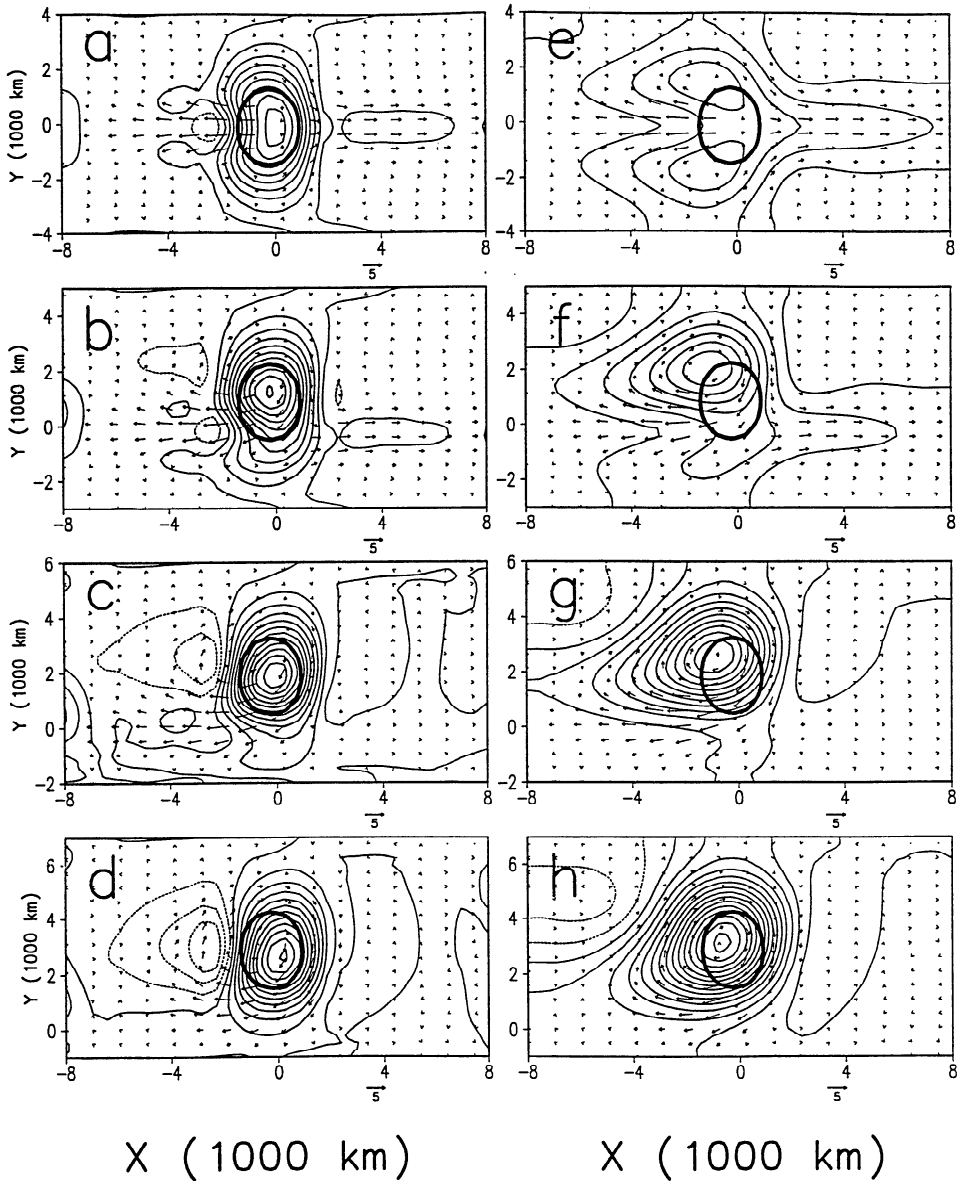

Figure 8. Same as Figure 3 except at a z= 9.5 km. The contour intervals of w and p in Figures 8a-8h are 0.0004 ms^{-1} and 30 Pa, respectively.

difference for the cases with elevated heating, the dramatic difference between Figures 10a and 10d is due to a smaller ε ($1.14x10^{-6}$ s^{-1}) and a much longer (30 d) forcing. The strength of the low pressure is also enhanced as the heating center is located at a higher latitude (Figures 10e-10h) due to the effect of increased vortex stretching. It is important to note that the low-level horizontal distribution of the vertical velocity induced by the surface heating is also similar to that of elevated heating. The differences in the vertical velocity fields at different latitudes may be explained by the divergence produced from the variation of the horizontal vector wind. As described in the last section, the low-level convergence induces upward motion which increases with height due to mass continuity and the constraint of no vertical motion at the surface.

Figure 11 shows the fields of vertical velocity and perturbation pressure on the x-z plane across the heating center. When the heating center is located at the equator (Figure 11a), the maximum vertical velocity tilts to the east with height. On the other hand, it tilts to the west with height when the heating center is located at higher latitudes, that is, 10°N, 20°N, and 30°N (Figures 11b-11d). The vertical phase tilt can be explained by the $\exp(i\lambda_r z)$ term as discussed in the last section. When the heating center is located at a higher latitude, the vertical velocity maximum is higher and the disturbance extends to greater heights. This is due to the increase in the vertical wavelength of the disturbance when f_o increases and β decreases as also explained in last section.

The heat-induced low pressure weakens exponentially with height to the level of maximum vertical velocity and then it becomes positive pressure perturbation, similar to cases of elevated heating (Figures 11e-11h). Notice that the magnitude of perturbation pressure (vertical motion) is larger (smaller) when the heating center is located at a higher latitude due to the vortex stretching effects as described in last section.

Figure 12 shows the y-z vertical cross sections of the vertical velocity and perturbation pressure fields. It is interesting to note that the vertical velocity maximum is located near the equator at the surface and is located near the latitude of the heating center at

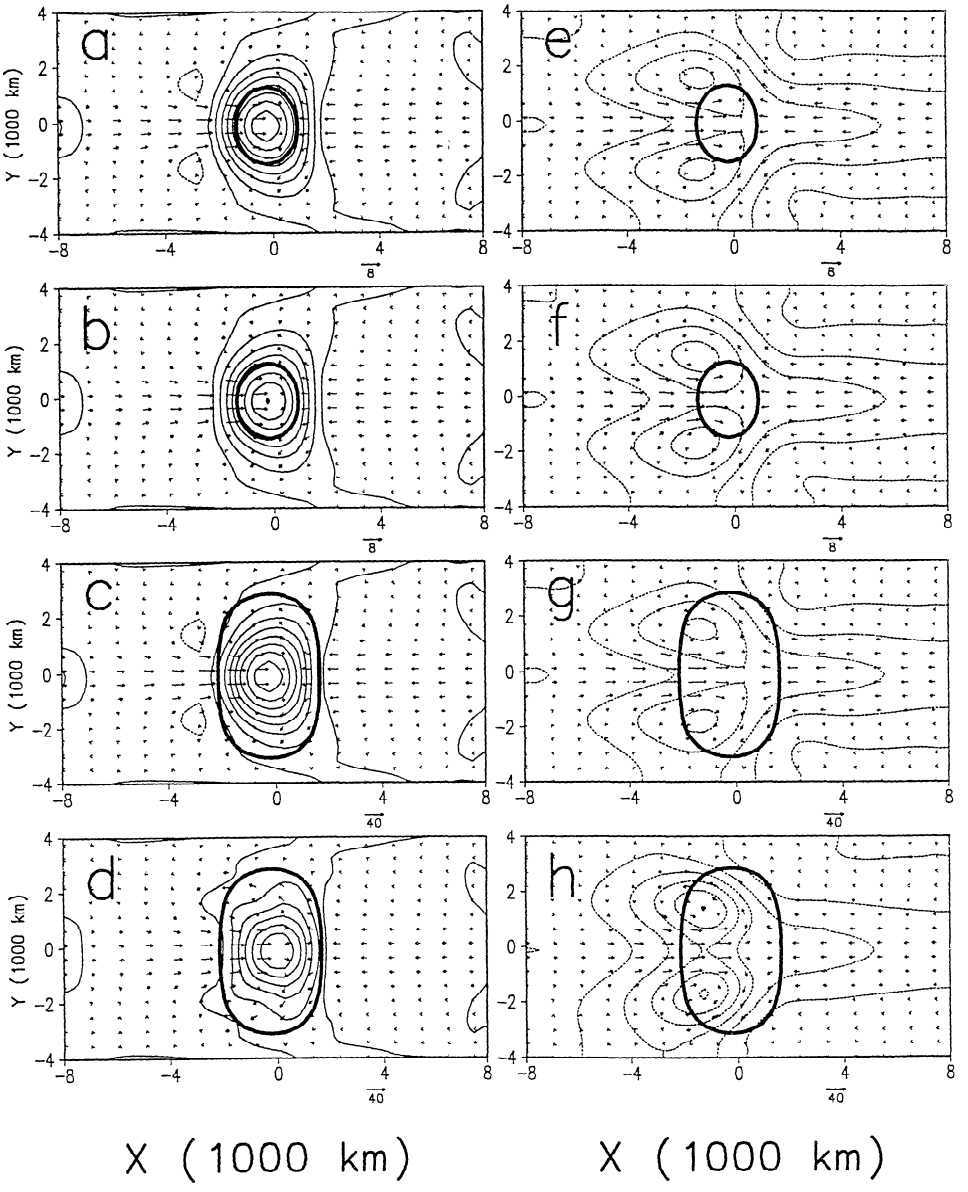

Figure 9. The vertical velocity and perturbation pressure fields for a linear response (Figures 9a and 9e) and for a nonlinear response (Figures 9b and 9f) for the case of Figure 3a. Corresponding fields are shown in Figures 9c and 9g for a linear response and for a nonlinear response (Figures 9d and 9h) for a case with a heating rate 5 times larger. The contour intervals of w and p are 0.0002 ms^{-1} and 50 Pa for Figures 9a, 9b, 9e and 9f and 0.001 ms^{-1} and 250 Pa for Figures 9c, 9d, 9g and 9h, respectively.

higher levels for every case (Figures 12a-12c). At the southern boundary, in the case with heating centered at 30°N (Figure 12d), there exists a region of weak vertical velocity which is due to the reflection from the southern boundary. Unlike the *w* fields, the vertical structure of the perturbation pressure field in the *y-z* plane are not very sensitive to the locations of heating source (Figures 12e-12h).

On the basis of the linear theory, the structure of thermally induced disturbances due to heating and cooling should be identical except with opposite signs. This can be seen from both vertical velocity and pressure fields for the linear responses to the surface heating (Figures 13a and 13e) and cooling (Figures 13b and 13f). However, the nonlinear responses due to heating (Figures 13c and 13e) and cooling (Figures 13d and 13h) are different in both structure and sign. *Liu and Schurmans* [1993] suggested that the nonlinear response to heating is stronger than the linear response, whereas the nonlinear response to cooling is weaker. Comparing the nonlinear and linear responses, we find that the magnitudes of disturbances induced by heating (cooling) are enhanced (reduced) by nonlinear effects, however, the disturbed area induced by heating (cooling) is reduced (enlarged) by the nonlinear effects (Figure 13). For example, the strongest downward velocity of the nonlinear response induced by surface cooling (Figure 13d) is weaker than that of the linear response (Figure 13b). Note the disturbed area is contracted to a narrower region for the heating case (Figure 13c), while it expands to a wider region for the cooling case (Figure 13d). This may be explained by the spreadout of downward moving air near the lower rigid surface.

The nonlinear effects are investigated by inspecting the nonlinear terms, that is, $u\partial u/\partial x$, $v\partial u/\partial y$, $w\partial u/\partial z$, $u\partial v/\partial x$, $v\partial v/\partial y$, $w\partial v/\partial z$, $u\partial\theta/\partial x$, $v\partial\theta/\partial y$, and $w\partial\theta/\partial z$, for both heatin

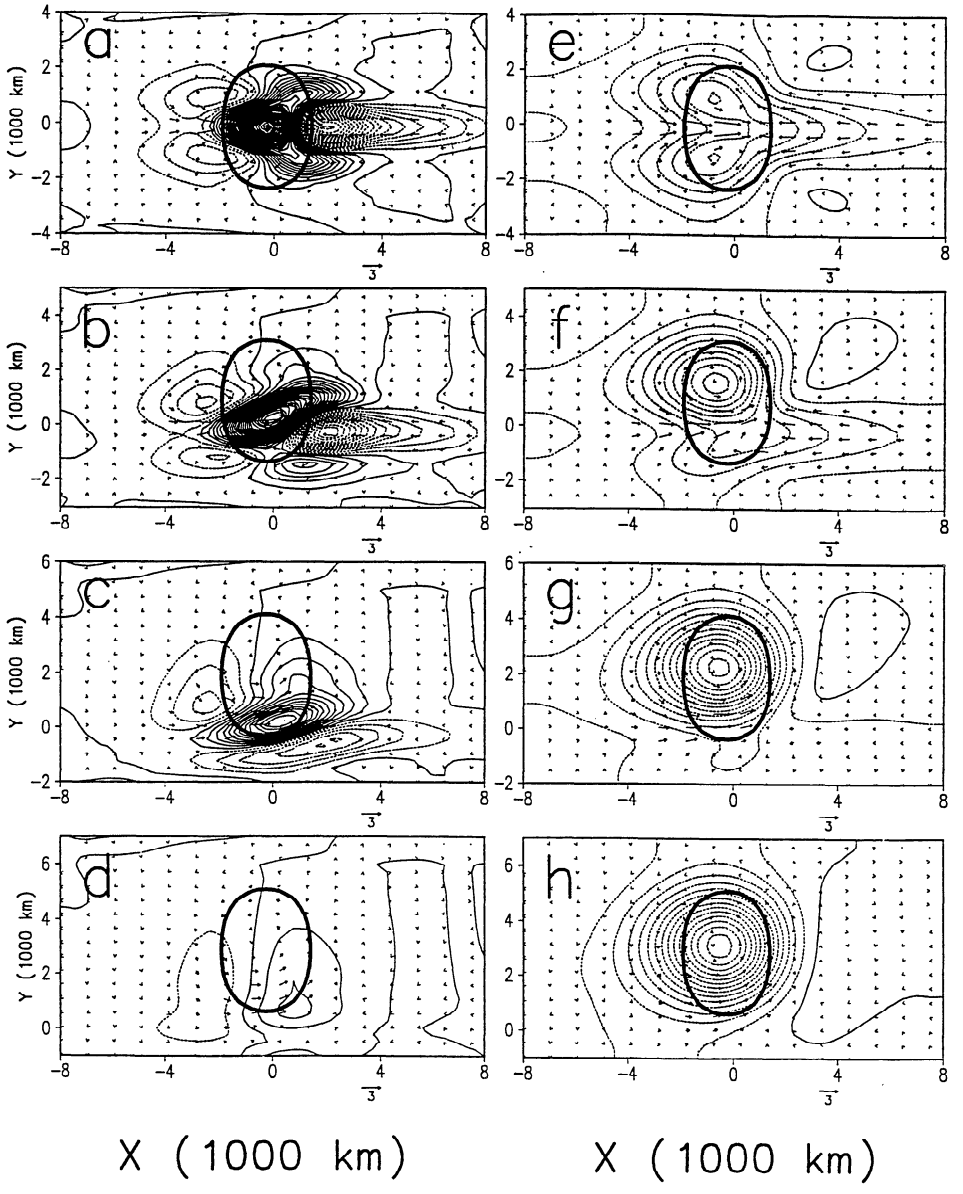

Figure 10. The horizontal perturbation vector wind, vertical velocity (thin contour lines on left panels, in meters per second), and the perturbation pressure (thin contour lines on right panels, in pascal) at $z = 500$ m for a low-level heating (thick solid line), which is specified by (16), (a, e) centered at the equator, (b, f) 10°N, (c, g) 20°N, (d, h) 30°N after 30 days. The ε is 1.14×10^{-6} s^{-1}. The contour intervals of w and p are 0.0001 ms^{-1} and 10 Pa, respectively.

and cooling cases (Figures 14 and 15). These terms may be lumped into the right-hand sides of (1), (2), and (3) and regarded as the forcing terms. In the heating case, the advection of the zonal wind (Figure 14d) tends to accelerate (positive $\partial u/\partial t$) the air near the heating center, while the temperature advection (Figure 14l) acts as an additional weak heat sink to the system. The advection of v wind (Figure 14h) acts to establish a couplet of convergence and divergence near the heating center, which strengthens the westerly jet there. The overall nonlinear effect in the heating case is to strengthen the disturbance and to diminish the spatial extent of the disturbance. In the cooling case, both the advection of the zonal wind and temperature (Figures 15d and 15l) are dominated by the vertical advection terms (Figures 15c and 15k). The advection of the zonal wind tends to accelerate the air on the left side of heating center toward the heating center. This is just in the opposite direction of the westward moving flow induced by cooling. Thus it tends to weaken the disturbance. Similarly, the disturbance is weakened by the nonlinear temperature advection (Figure 15l) which acts as an additional strong heat source. The advection of v wind (Figure 15h) is almost negligible compared with the advection of u and θ fields. In other words, the overall nonlinear effect in the cooling case is to weaken the disturbance. Both nonlinear advection terms are spread to a wider area, which are responsible for the wider disturbance. The nonlinear effects for cases with heating centered at a higher latitude (e.g., 20°N) are similar (Figure 16).

Another interesting phenomenon is that the difference between the linear and nonlinear response is larger when the thermal forcing is located at a lower latitude. This can also be explained by comparing different terms in the x momentum

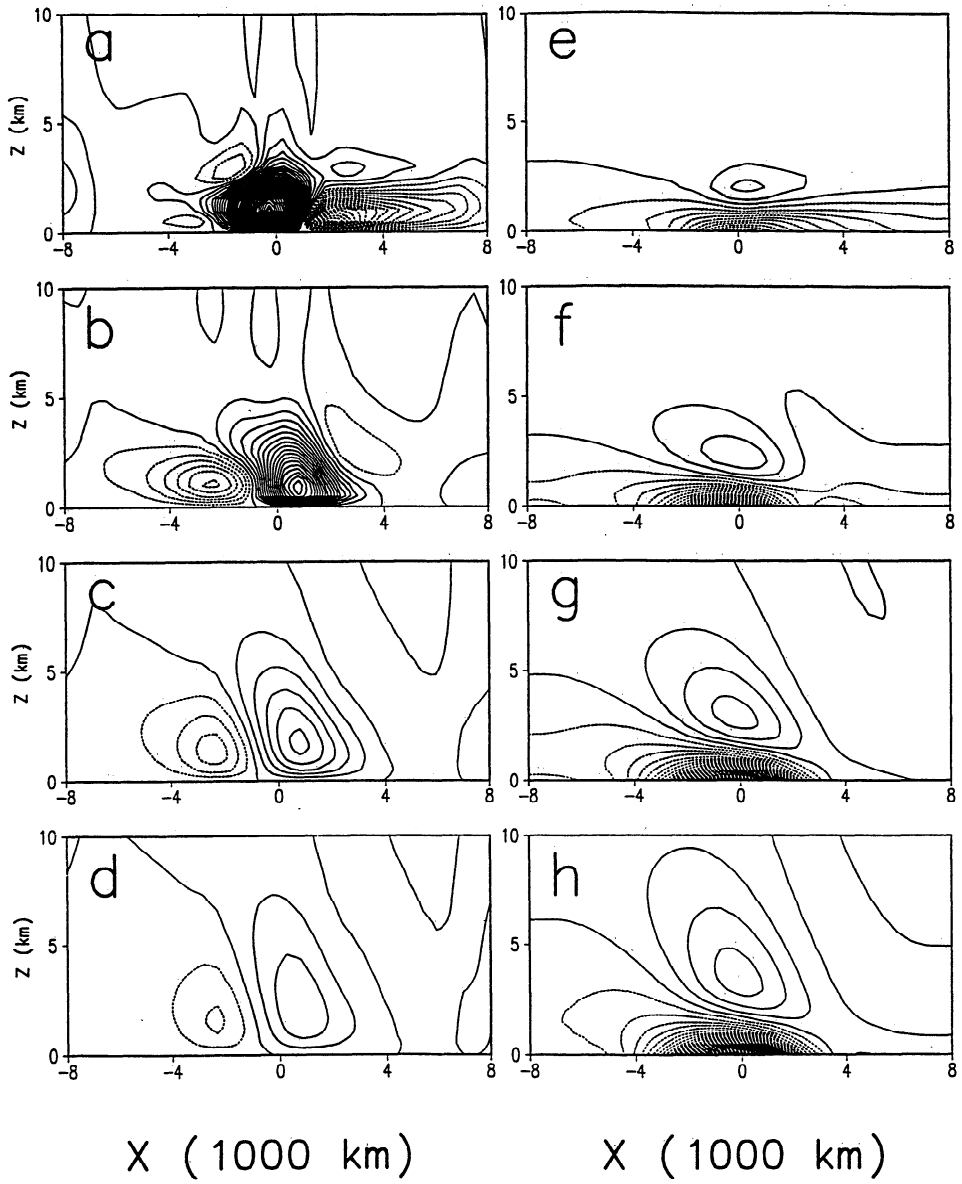

Figure 11. (left) The x-z vertical cross sections of vertical velocity and (right) perturbation pressure along the latitude of the heating center for cases of Figure 10. The contour intervals of w and p are 0.0001 ms^{-1} and 10 Pa, respectively.

equation for the cases of Figure 10 (Figure 17). When the heating center is located at a higher latitude, both the nonlinear advection term (term B, $u\partial u/\partial x$), and the Rayleigh friction term (term D, εu) are smaller, but the Coriolis force term (term C, fv) is larger. When the heating is centered at 30°N, the magnitudes of the Coriolis force term and pressure gradient force term (term E) are almost equal (Figure 15d), that is, the two forces are almost in geostrophic balance. This also supports the validity of the quasi-geostrophic approximation which is often applied to study meteorological phenomena in midlatitudes.

5. The Influence of Atlantic SSTA on Wind Patterns in Brazil and the Sahel

In this section, we investigate the effects of the Atlantic SSTA on the wind patterns in the African Sahel and northeastern Brazil. The SSTA are represented by prescribed diabatic forcings in the following numerical simulations. The diabatic forcing rate corresponding to SSTA have been discussed by *Egger* [1977] and *Webster* [1981] which suggested that a +1 K SSTA leads to a warming of 0.3-1.0 K d^{-1} for the overlying atmospheric column. These correspond to a forcing rate of 0.0035-0.0116 J $kg^{-1}s^{-1}$. In this study, we use the upper limit of their estimate and assume an 1.4 K SSTA which corresponds to a diabatic forcing rate of 0.016 J $kg^{-1}s^{-1}$.

The diabatic forcing function used to simulate the SSTA distribution is specified as

$$Q(x,y,z)=Q_1\left[\frac{y-y_o}{b}\right]\exp\left[\frac{-(x-x_o)^2}{4a^2}\right]$$

$$\exp\left[\frac{-(y-y_o)^2}{4b^2}\right]\exp\left[\frac{-z}{H_1}\right] \quad \text{for } y>y_o \tag{17a}$$

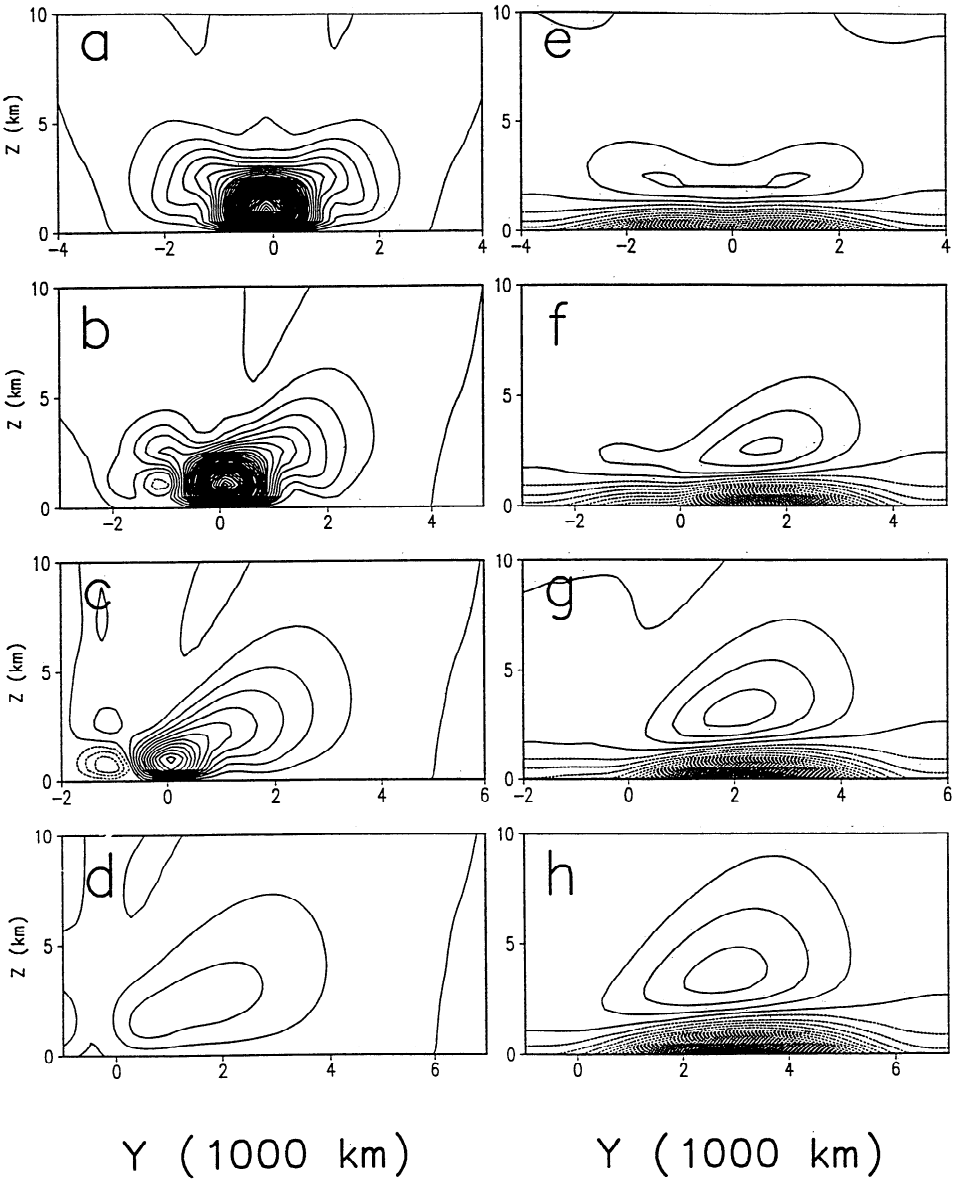

Figure 12. (left) The y-z vertical cross sections of vertical velocity and (right) perturbation pressure at x=0 for cases of Figure 10. The contour intervals of w and p are 0.0001 ms^{-1} and 10 Pa, respectively.

$$Q(x,y,z)=Q_2\left[\frac{y-y_o}{b}\right]\exp\left[\frac{-(x+x_o)^2}{4a^2}\right]$$

$$\exp\left[\frac{-(y-y_o)^2}{4b^2}\right]\exp\left[\frac{-z}{H_1}\right] \quad \text{for } y<y_o \tag{17b}$$

where x_o=1500 km, y_o=1000 km, a=1000 km, b=1000 km, and H_1=1 km. The diabatic forcing rates, Q_1 and Q_2, are summarized in Table 1. The choice of this type of SSTA distribution is based on the dominant observational SSTA patterns [e.g., *Moura and Shukla*, 1981]. Recently, *Semazzi et al.* [1995] have investigated the coupled variability between the African continental rainfall and global SSTA using the singular value decomposition technique (SVD). They found that the climate variability of the Sahelian summer rainfall is dominated by two distinct coupled SST/rainfall modes. One of these regimes, the flip-flop mode, is characterized by opposite phase in the rainfall anomalies between the equatorial region and the subtropical regions while the second one, the Sahel mode, is primarily confined to the northern hemisphere. The Sahel oscillation features ultralong timescale of possibly up to 100 years. The flip-flop mode also has an interdecadal timescale but shorter than the Sahel mode. The corresponding SSTA patterns share several common characteristics, such as having the same sign of anomalies prevailing over most of the tropical belt. The main difference between them are the different SSTA anomaly spatial characteristics over the Atlantic ocean. The SSTA pattern corresponding to the flip-flop mode is more pronounced in North Atlantic ocean sector while the Sahel mode has a stronger signal in the southern Atlantic. Warm/cold SSTA conditions over the South/North Atlantic yield drought conditions over the Sahel. The joint contribution of these two modes over the Atlantic

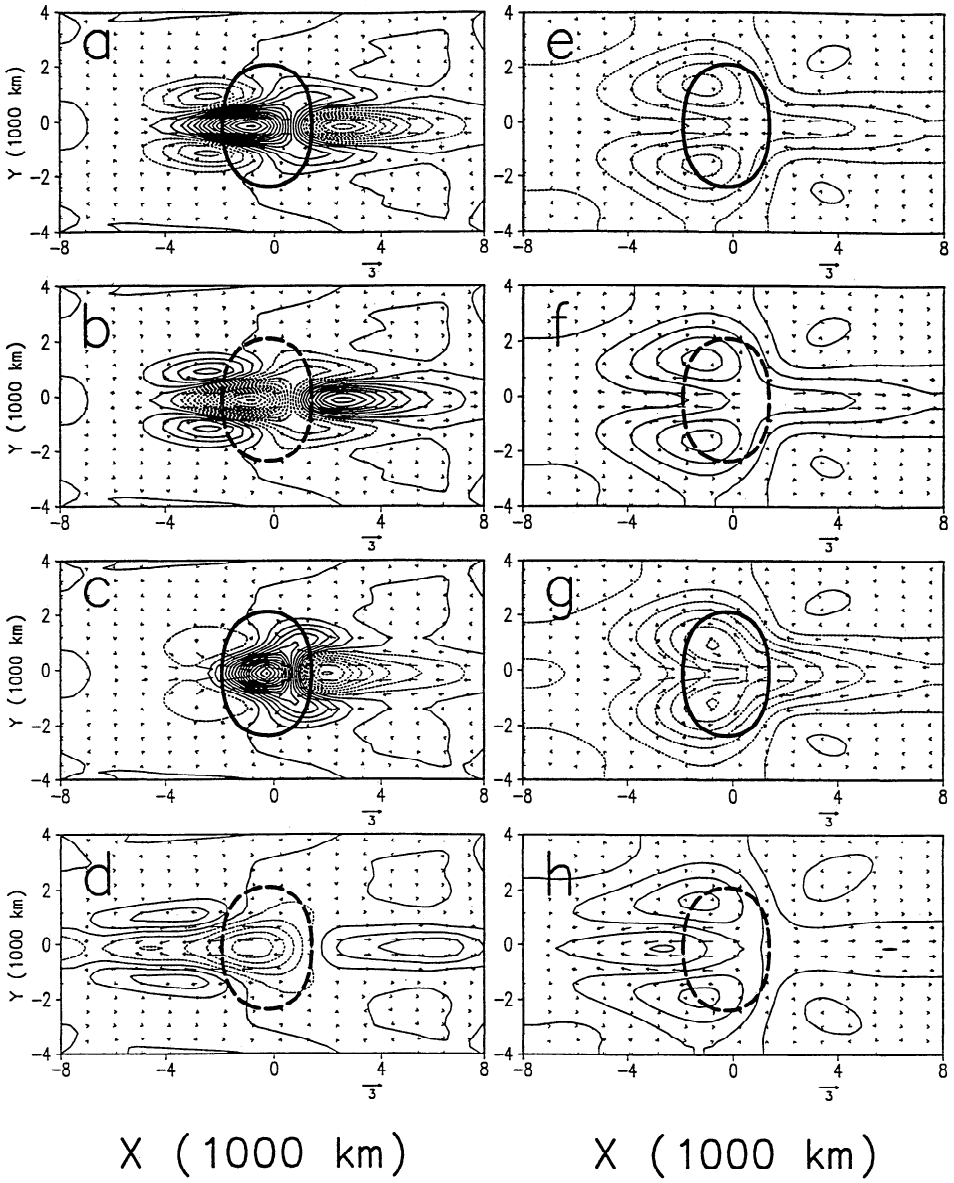

Figure 13. The horizontal perturbation vector wind field, vertical velocity (thin contour lines on left panels, in meters per second), and the perturbation pressure (thin contour lines on right panels, in pascal) at z= 500 m for a low-level heating (thick line) centered at the equator after 30 days. They are linear (a, e) simulation for heating; (b, f) linear simulation for cooling; (c, g) nonlinear simulation for heating; and (d, h) nonlinear simulation for cooling. The contour intervals of w and p are 0.0002 ms^{-1} and 10 Pa, respectively.

ocean corresponds to the south-north SSTA dipole usually implicated in the perpetuation of the severe Sahelian droughts. Before investigating the more complicated problem of rainfall anomalies induced by SSTA, we will study the impact of SSTA on the wind patterns in adjacent continents since these wind patterns affects the moisture supply which, in turn, affects the regions of convection. In the vertical distribution of the diabatic forcing, we use an exponentially decaying function which represents the surface sensible heating instead of elevated latent heating since we are interested in the process before deep convection develops.

The numerical parameters used in this section are: Δx=400 km, Δy=300 km, Δz=500 m, Δt=3 min. There are 64x32x21 grid points. The ε is taken to be the same as in low-level heating case, that is, 1.14×10^{-6} s^{-1}. The numerical results are superimposed on a geographical map background in order to describe responses more clearly.

5.1. Warm SSTA in the South Atlantic

Figure 18 shows the response at z=500m to a warm SSTA in the South Atlantic. The warmest SSTA is specified at the location near (5°W, 13°S). The results show a strong upward motion in the region between the SSTA center and the equator. Weaker compensating downward motion occurs in two regions: one enclosed by the equator, 10°N, 30°W, and 40°E and the other in the vicinity of (22°W,15°S). We will focus the discussion on the response near northeastern Brazil region and the African Sahel region which are prone to drought condition. As mentioned earlier, the Sahelian region is defined as the region

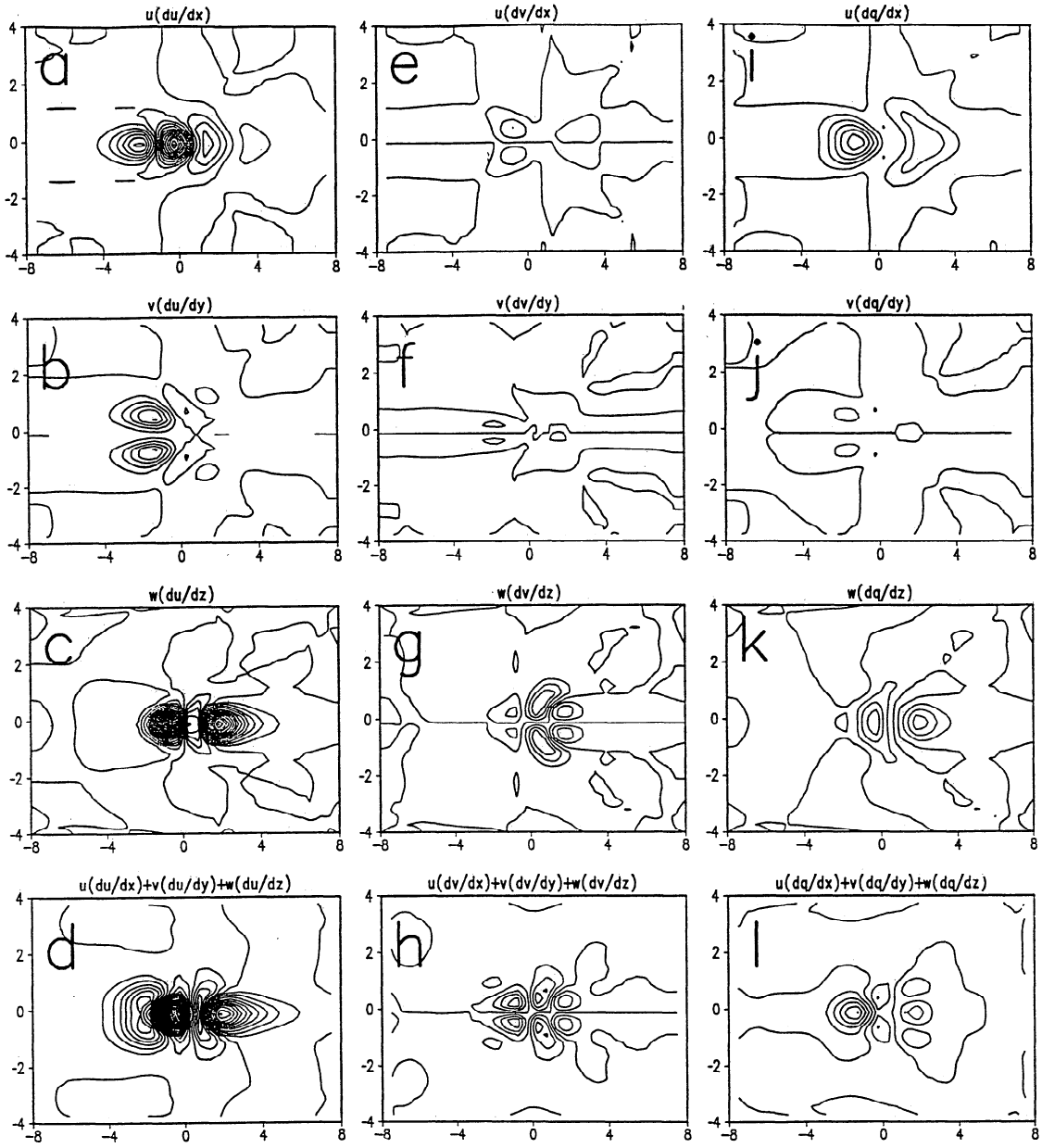

Figure 14. Fields of nonlinear terms for the low-level heating case of Figure 10: (a) $u\partial u/\partial x$, (b) $v\partial u/\partial y$, (c) $w\partial u/\partial z$, (d) $u\partial u/\partial x+v\partial u/\partial y+w\partial u/\partial z$, (e) $u\partial v/\partial x$, (f) $v\partial v/\partial y$, (g) $w\partial v/\partial z$, (h) $u\partial v/\partial x+v\partial v/\partial y+w\partial v/\partial z$, (i) $u\partial\theta/\partial x$, (j) $v\partial\theta/\partial y$, (k) $w\partial\theta/\partial z$, (l) $u\partial\theta/\partial x+v\partial\theta/\partial y+w\partial\theta/\partial z$.

between 10°N and 20°N in North Africa. It can be seen from Figure 18a that the response in the Sahel region and in northeastern Brazil are very weak. In the Sahelian region, the results show a weak easterly wind which blows offshore. This can act to decrease the moisture supply for the Sahel region. The flow direction is also offshore in the northeastern Brazil region.

As described in last section, the vertical velocity maximum coincides with the heating center only when the heating is centered at the equator. When the heating is centered at a higher (lower) latitude, the vertical velocity maximum is shifted to the southeast (northeast) of the heating center due to the β effect. In addition, the vertical velocity maximum almost coincides with the jet in the lower layer. In the present case, the heating center is located at 15°S. Therefore the maximum upward velocity occurs to the northeast of the heating center and almost coincides with the jet (Figure 18). This is consistent with earlier results.

It may be reasonable to hypothesize that the rainfall would tend to increase in a region with upward motion and onshore flow since there then exists a moisture supply for the upward motion to trigger convection, rainfall should decrease in a region with downward motion and offshore flow. In the present case, both the response in the African Sahel and in northeastern Brazil are very weak. Since the horizontal vector wind fields in these two regions are both offshore, they tend to decrease the moisture supply and may be expected to reduce the chance of convection in these two regions. The GCM results of *Druyan* [1987, 1989] suggested that a warm SSTA in the southeastern Atlantic may reduce the rainfall over North Africa by lowering atmospheric

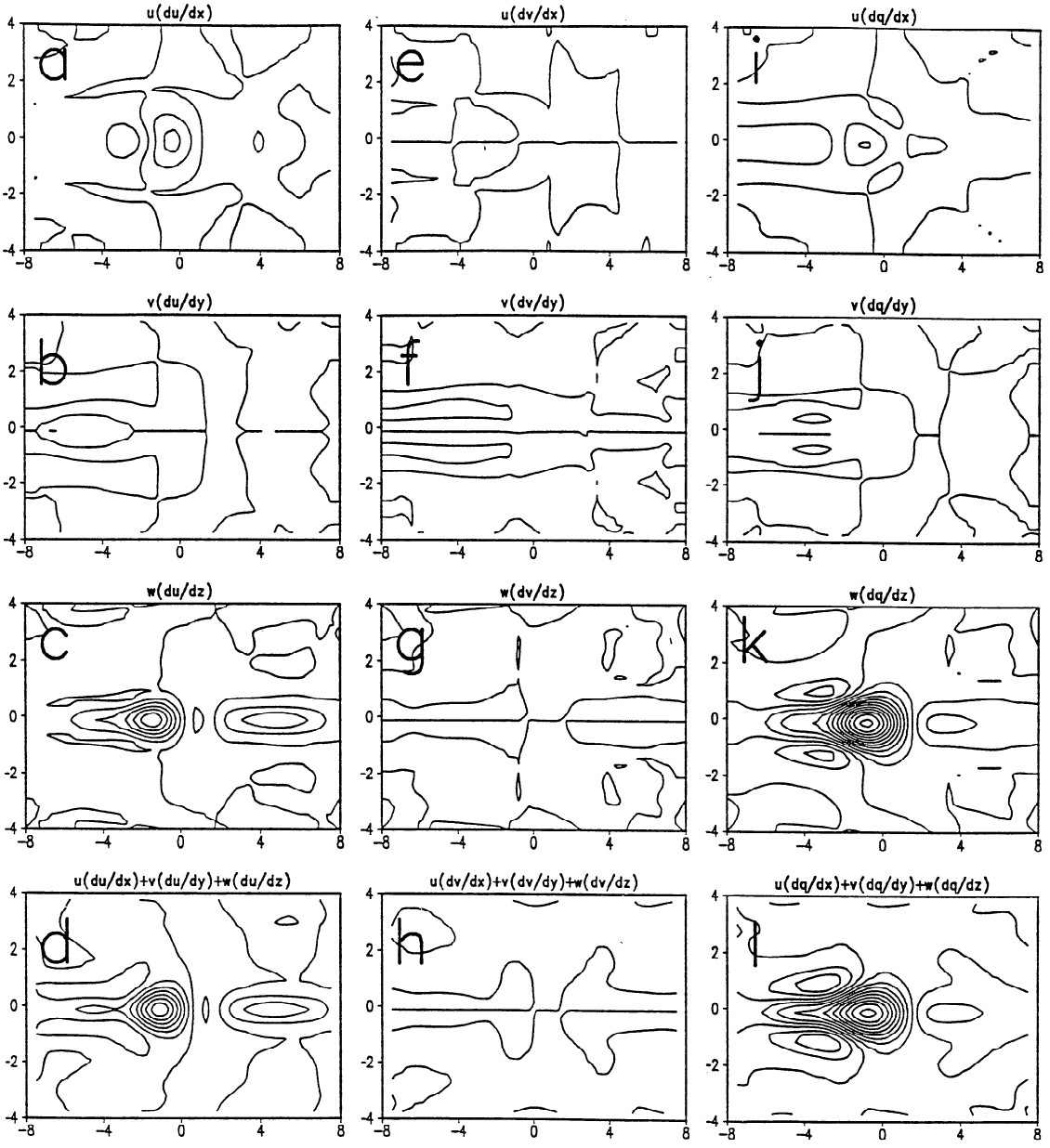

Figure 15. Same as Figure 14 except for the cooling case.

pressures, thereby weakening the moisture-laden southerly flow along the southwest coast of Africa. The present study provides evidence for the existence of the above mechanism in a simple idealized atmosphere.

5.2. Warm SSTA in the North Atlantic

Figure 19 shows the response at z=500m to a warm SSTA in the North Atlantic. The warmest SSTA is specified at the location near (33°W, 13°N). The maximum upward velocity occurs to the southeast of the heating center (Figure 19a) due to the β effect, as discussed in previous sections. There exists weak upward motion in the west Sahel and downward motion over the central part of northeastern Brazil. Different rainfall regimes in northeastern (NE) Brazil have been identified as north (NNE), south (SNE) and east (ENE) part of northeastern Brazil [e.g. *Rao et al.*, 1992]. In this study, we focus only on ENE when we discuss the tendency of rainfall of northeastern Brazil since the responses there are stronger than the other two regions. Figure 19b shows the heating induced horizontal vector wind field. The results show a anticlockwise circulation in the North Atlantic. A westerly jet occurs to the south of the heating center, which also coincides with the vertical velocity maximum. Near the west Sahelian region, there exists a southwesterly onshore flow. In the northeastern Brazil, there exists an easterly onshore flow near 10°S and southwesterly offshore flow near 3°S.

In the present case with a warm SSTA in the north Atlantic, results indicate an upward motion and a southwesterly onshore flow near the west African Sahel. This situation may result in a positive rainfall anomaly pattern in the western Sahel based on our hypothesis. On the other hand, the onshore flow in northeastern Brazil may increase the moisture supply. However, the downward motion may tend to suppress convection and produces a negative rainfall anomaly there.

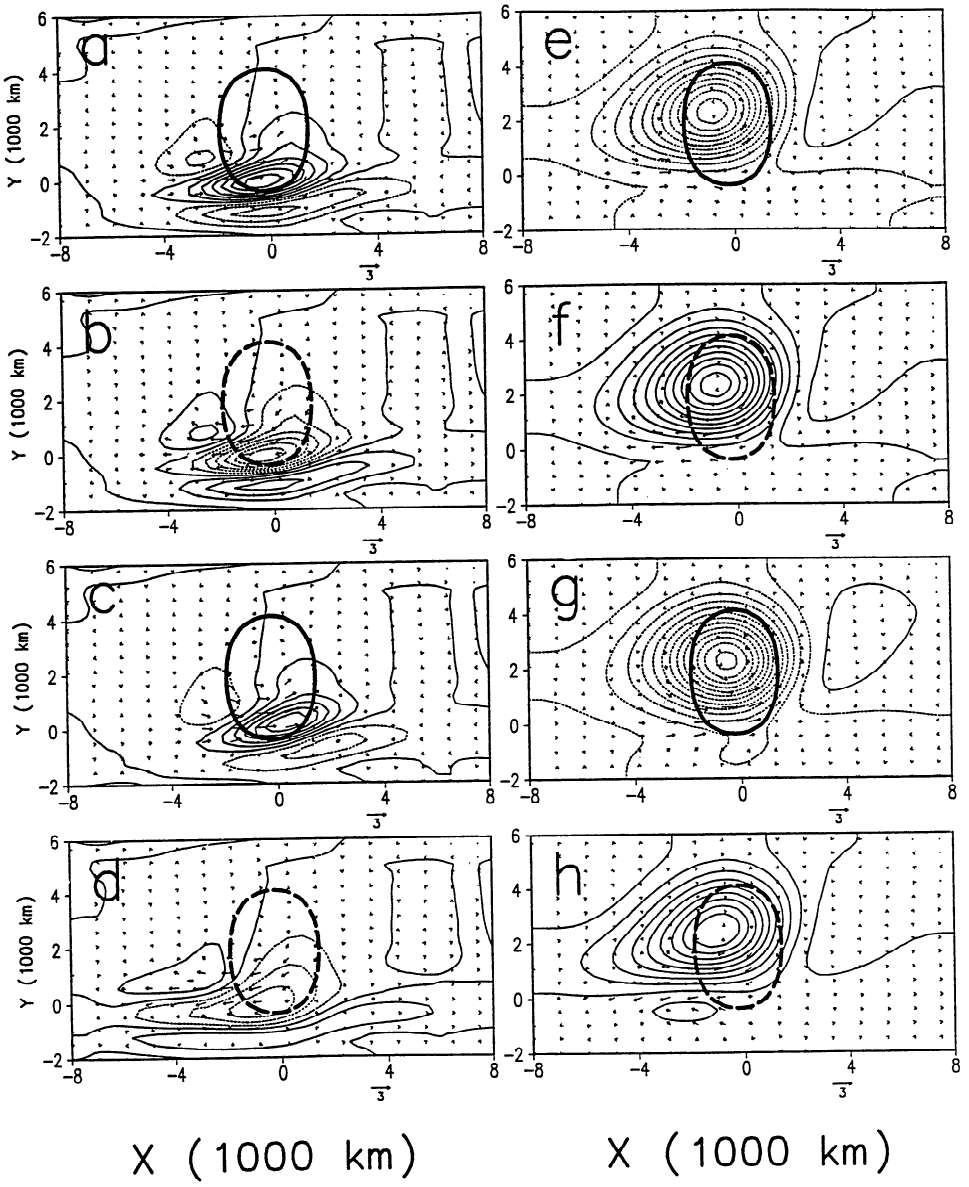

Figure 16. Same as Figure 13 except for thermal forcing centered at 20°N. The contour intervals of w and p are 0.0002 ms^{-1} and 10 Pa, respectively.

5.3. Cold SSTA in the South Atlantic

Figure 20 shows the response at z=500m to a cold SSTA in the South Atlantic. All the parameters adopted in the numerical model for this case are exactly the same as those used in the case of Figure 18 except for the sign of Q_2 (17b). However, the disturbed areas of these two cases are very different. The response in the warm SSTA case (Figure 18) is more confined in the vicinity of the heating region. However, the disturbed area extends to a much larger region in the east-west direction in the present case (Figure 20a). The strongest downward motion occurs near (6°W, 6°S) which is to the north of the cooling center. The region of downward motion extends to 60°W in the west and 25°E in the east. There are two regions of compensating upward motion, one is to the west of the cooling region and the other primarily in the northern hemisphere with an elongated east-west extent. The significant difference between Figures 20 and 18 can be explained by the nonlinear effects as described in section 4. As shown in Figures 13a-13d, the linear results of heating (Figure 13a) and cooling (Figure 13b) have exactly the same structure except that the signs are opposite. However, the corresponding nonlinear result for the low-level heating (Figure 13c) has a stronger disturbance but with a smaller disturbed area. However, the corresponding nonlinear result for cooling (Figure 13d) has a weaker response but with a larger disturbed area. The strongest upward velocity is 0.0005 ms^{-1} in Figure 20a, while it is 0.0017 ms^{-1} in Figure 18a. A portion of the Sahelian region is covered by the upward motion. Most of the northeastern Brazil is covered by downward motion. The cooling induced horizontal vector wind field is shown in Figure 20b. Our results show a strong easterly jet over the equatorial Atlantic ocean. In the northeastern Brazil, this easterly onshore flow is very strong. The wind in the Sahel is very weak upwards and onshore.

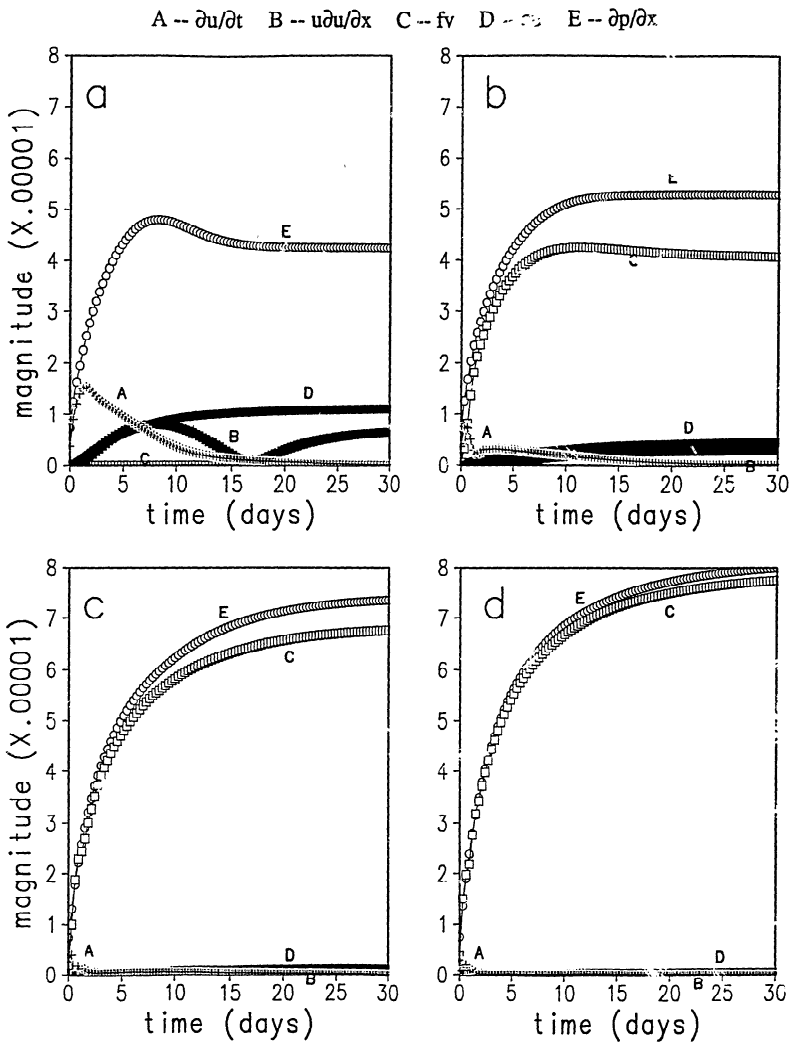

Figure 17. The time evolution of different terms in zonal momentum equation at (x= -1000 km, y=the latitude of heating center, z=0 m) for cases of Figure 10. Symbols A, B, C, D, and E denote $\partial u/\partial t$, $u\partial u/\partial x$, fv, εu, and $\partial\phi/\partial x$, respectively. The heating center is located at the (a) equator, (b) 10°N, (c) 20°N, and (d) 30°N.

The results show a strong easterly onshore flow and a strong downward motion in northeastern Brazil. Therefore, the convections in these two regions may be weak for a cold SSTA in the South Atlantic ocean if they exist.

5.4. Cold SSTA in the North Atlantic

Figure 21 shows the response at z=500 m to a cold SSTA in the North Atlantic. Similar to the previous case, the disturbed area is much larger than that of the corresponding heating case. This region of downward motion extends further to the west to 90°W in the equatorial area. Compensating upward motion occurs to both the south and west of the cooling region. The region of upward motion to the south of the cooling region is also elongated in the zonal direction. The vertical velocity maximum occurs in the northeastern Brazil. There also exists a downward motion in the western Sahel. The easterly jet occurs in the equatorial area to the southwest of the cooling region (Figure 21b). The flow exhibits an anticyclonic circulation in the North Atlantic. There exists a strong easterly onshore flow in the northeastern Brazil. The horizontal wind near the Sahel is very weak.

Since the results show an upward velocity to enhance convection in addition to an easterly onshore flow which supplies the moisture in the northeastern Brazil, it may produce more convection and possibly a positive rainfall anomaly in this region. On the other hand, the downward motion and weak horizontal wind in the western Sahel tend to reduce the chance of convection and possibly the amount of rainfall.

Table 1: The Values of Q_1 and Q_2 for Numerical Simulations in Section 5

SSTA Distribution	Q_1	Q_2
Warm SSTA in the South Atlantic	0.	0.016
Warm SSTA in the North Atlantic	0.016	0.
Cold SSTA in the South Atlantic	0.	-0.016
Cold SSTA in the North Atlantic	-0.016	0.
Warm (cold) SSTA in the South (North) Atlantic	-0.016	0.016
Warm (cold) SSTA in the North (South) Atlantic	0.016	-0.016

Q_1 and Q_2 are measured in joules per kilogram per second.

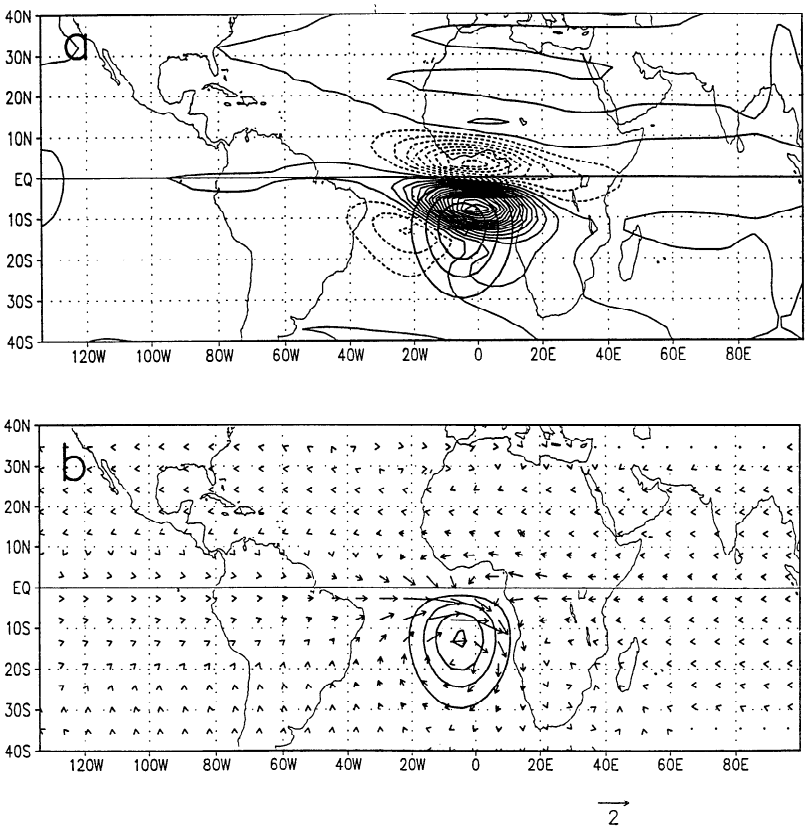

Figure 18. The vertical velocity (thin contour lines on a, in meters per second) and horizontal perturbation vector wind (b) at z = 500 m for warm SSTA (thick lines) in South Atlantic after 30 days. The SSTA is specified by a heating funcation described by (17). The interval of vertical velocity contour is 0.0001 ms^{-1}.

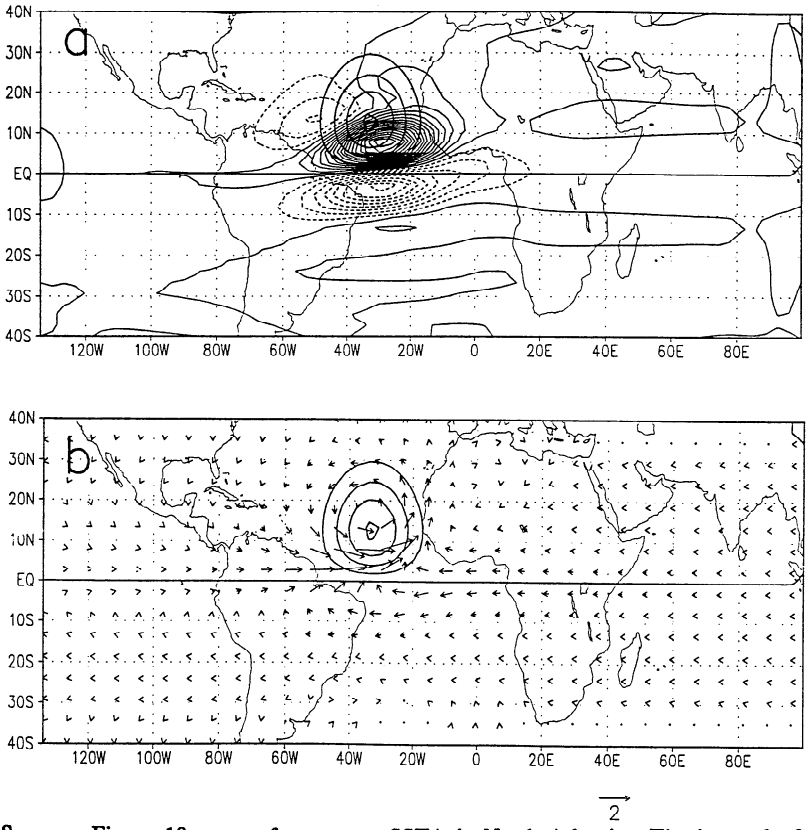

Figure 19. Same as Figure 18 except for a warm SSTA in North Atlantic. The interval of vertical velocity contour is 0.0001 ms^{-1}.

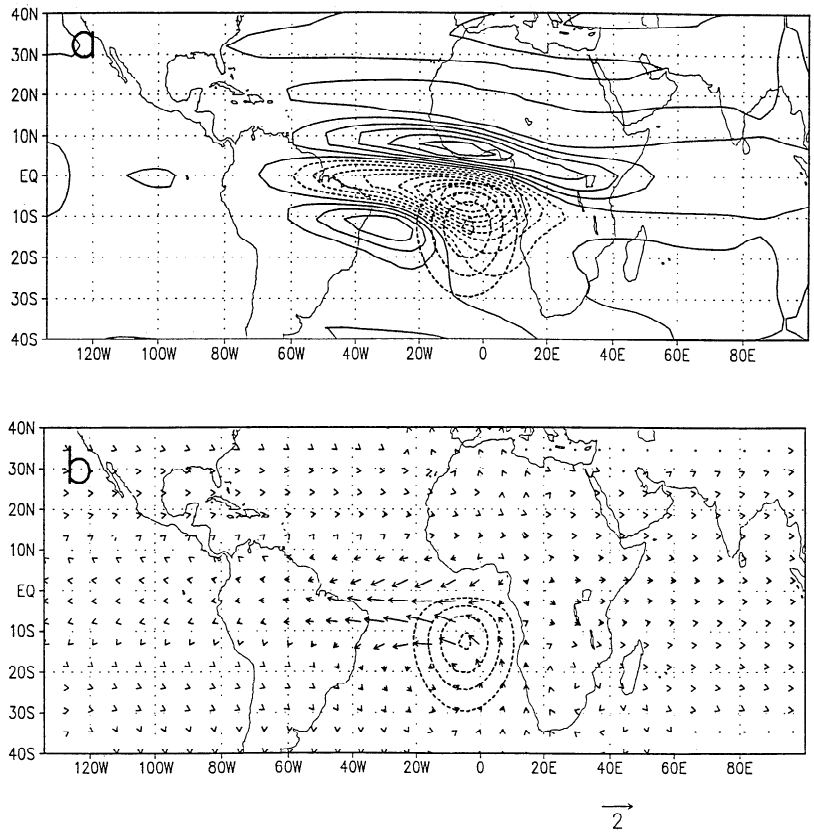

Figure 20. Same as Figure 18 except for a cold SSTA in South Atlantic. The interval of vertical velocity contour is 0.0001 ms^{-1}.

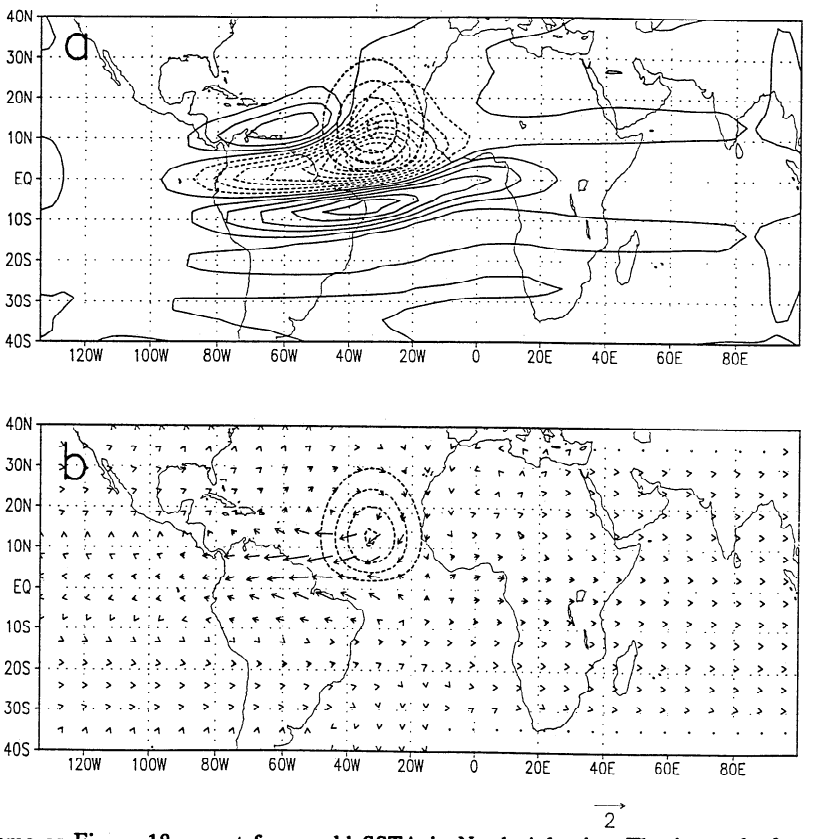

Figure 21. Same as Figure 18 except for a cold SSTA in North Atlantic. The interval of vertical velocity contour is 0.0001 ms^{-1}.

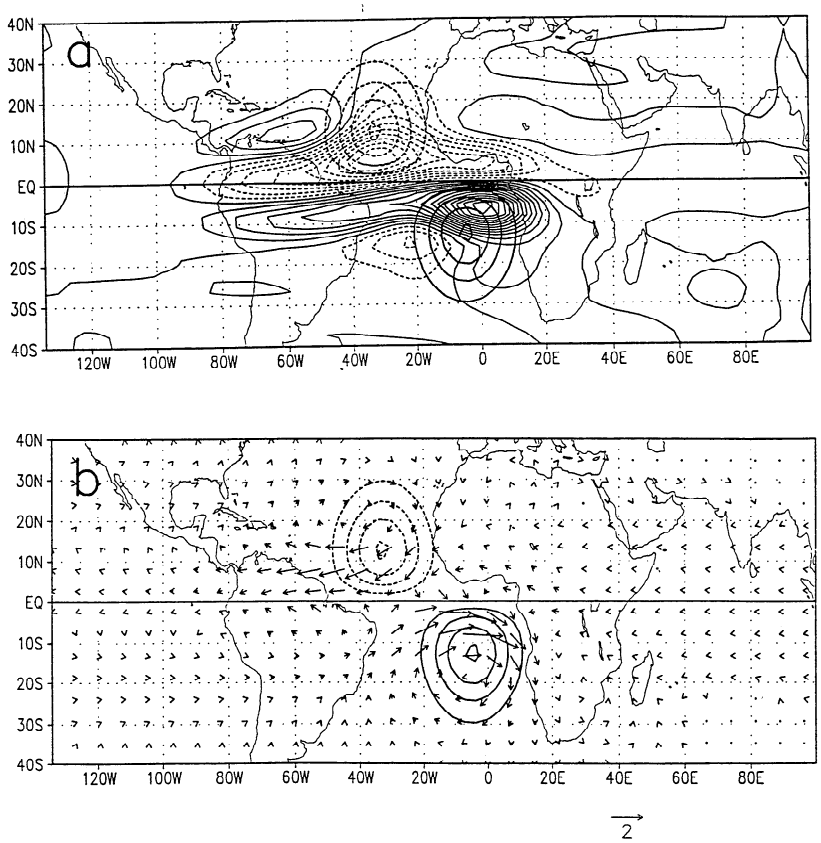

Figure 22. Same as Figure 18 except for a couple warm SSTA in South Atlantic and cold SSTA in North Atlantic. The interval of vertical velocity contour is 0.0001 ms^{-1}.

5.5. Warm SSTA in the South Atlantic and Cold SSTA in the North Atlantic

Figure 22 shows the response at z=500m to a coupled warm SSTA in the South Atlantic and cold SSTA in the North Atlantic. The model shows a downward motion in the tropical northern hemisphere near the cooling region and an upward motion in the tropical southern hemisphere near the heating region (Figure 22a). The response in the west Sahel is a very weak downward motion, while there is a weak upward motion in the northeastern Brazil. There exists an easterly jet to the southwest of the cooling region and a westerly jet to the north of the heating center (Figure 22b). These flows form an anticyclonic circulation in the North Atlantic and a cyclonic circulation in the South Atlantic, but the magnitude of the horizontal vector wind near the equator is much larger than that in higher latitudes. Both flows in the Sahel and northeastern Brazil are offshore. The combination of offshore flow and weak downward motion in the Sahel should be expected to reduce the chance of convection and possibly a negative rainfall anomaly.

Folland et al. [1986] and *Palmer* [1986] also suggested that the cold SSTA in the North Atlantic can combine with warm SSTA in the South Atlantic to promote a drought-prone monsoon circulation in the Sahel. In addition, *Lamb* [1978] provides observational evidence by the case study in 1968 which supports this hypothesis, and which is a dry year for the Sahel (Figure 1). During July-September 1968, the positive SSTA occurred in the South Atlantic, with a southwest-northeast oriented negative SST anomaly immediately to the northwest. Thus the response of an idealized atmosphere to a couplet of cold and warm SSTA is consistent with observations in the Sahel region. For the northeastern Brazil, the offshore flow tends to decrease the availability of the moisture supply, even though there exists a very weak upward motion. Under this situation, convections may be weak if they exist.

5.6. Cold SSTA in the South Atlantic and Warm SSTA in the North Atlantic

Figure 23 shows the response at z=500 m to a coupled cold SSTA in the South Atlantic and warm SSTA in the North Atlantic. The results show an upward motion in most of the heating region and a downward motion over most of the cooling region, although the extrema are located primarily between the forcing centers and the equator (Figure 23a). In the western Sahel, there exists a weak upward motion occurs. The downward motion in the southern hemisphere extends further to the west, and covers northeastern Brazil. Similar to the previous case, the magnitudes of the vector wind near the equator are much larger than those in higher latitudes (Figure 23b). The horizontal vector wind field in the western Sahel is dominated by southwesterly flow with a weak onshore component. The strongest wind speed occurs in tropical south Atlantic near the Brazilian coast and the direction of this jet is easterly. Therefore, onshore flow in northeastern Brazil occurs. The direction of the flow may be very important for the precipitation in the eastern part of northeastern Brazil according to *Rao et al.* [1992].

The existence of a weak onshore flow and an upward motion in the western Sahel may cause more convections and possibly a positive rainfall anomaly. Again, the case study of a wet year (1967), [see *Lamb,* 1978] indicated that the SSTA pattern for July-September 1967 includes positive anomalies west of West Africa and negative departures in the South Atlantic (Figure 1). In northeastern Brazil, although the onshore flow is very strong,

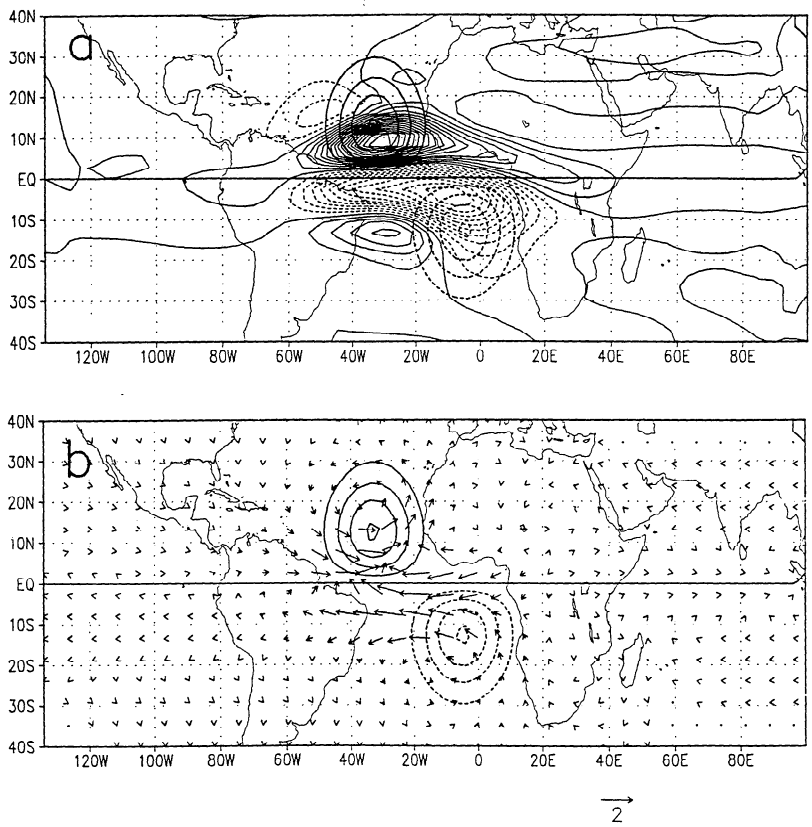

Figure 23. Same as Figure 18 except for a coupled warm SSTA in North Atlantic and cold SSTA in South Atlantic. The interval of vertical velocity contour is 0.0001 ms^{-1}.

the downward motion tends to suppress convection and possibly decrease the amount of rainfall there. This is consistent with the simulations of *Moura and Shukla* [1981] which indicated that simultaneous occurrences of warm SSTA in the North Atlantic and cold SSTA in the South Atlantic are associated with negative rainfall anomalies in the northeastern Brazil.

6. Concluding Remarks

The response of a stably stratified atmospheric flow to large-scale elevated and low-level thermal forcing on a β plane are investigated using a simple nonlinear numerical model. For elevated heating, the present results compare very well with theoretical solutions of *Gill* [1980]. Results of sensitivity tests to the coefficients of Rayleigh friction and Newtonian cooling and the basic wind velocities are similar to *Phlips and Gill* [1987]. The formation of a westerly jet at the equator, a pair of low-pressure regions and the corresponding cyclonic circulations, and the offset of the westerly jet and the heating center when the latter is located at higher latitudes, are explained by the β effect by studying the transient responses. The flow at a higher level is divergent due to the mass continuity despite the existence of diabatic heating at this level. It is found that the vertical motion in the case with heating centered at the equator is much larger than that in the case with heating centered at higher latitudes. This is explained by (1) there is much more rotational flow around the heating center at higher latitudes, which in turn produces less convergence and vertical motion, and (2) there is much more wave energy trapped in the equatorial plane when the heating is centered at the equator.

It is found that the constant phase of maximum vertical velocity tilts eastward with height for the case with heating centered at the equator, while it tilts westward for the case with heating centered at higher latitudes. The phase tilt is associated with the $\exp(i\lambda_r z)$ term based on the quasi-geostrophic approximation and can be explained by the wave propagation properties. In the former case, the disturbance is dominated by the Kelvin wave which tends to produce an eastward phase tilt because it propagates eastward. In the latter cases, the disturbance is dominated by the Rossby waves which tend to produce a westward phase tilt because it propagates westward. The vertical wavelength of the disturbance increases as the heating center is located at a higher latitude. Again, this is supported by the analysis based on the quasi-geostrophic dynamics. This also indicates that the rigid lid upper boundary condition, which is often adopted in large-scale dynamics, is more reasonable for studying problems in lower latitudes than in higher latitudes, such as that higher than 30°. In addition, we find that this type of flow is not sensitive to the existence of the stratosphere.

The basic features and structures of disturbances induced by prescribed low-level sensible heating are similar to those induced by prescribed elevated heating. One striking feature is that the maximum vertical velocity for the case with heating centered at the equator is more than 10 times larger than that with heating centered at 30°N. The stronger response for the former case has also been observed in the case with elevated heating. This is due to (1) a smaller ε and a much longer forcing time and (2) much more energy is projected on gravity wave modes with relatively small equivalent depth in the case of shallow heating near the equator compared to the deep heating. The highly internal gravity modes are sufficiently slow and therefore quasi-resonant with the stationary forcing. The vertical motion is stronger in the case of shallow heating near the equator because there modes

are highly divergent. Comparing both linear and nonlinear cases with surface heating or cooling, we find (1) the nonlinearity suppresses (enhances) the disturbance induced by cooling (heating), (2) the differences between the nonlinear and linear responses are larger when the forcing is located at lower latitudes, and (3) for cases with cooling centered off the equator, the disturbed areas are much wider in the zonal direction than for cases with heating since the downward moving air is forced to spread out horizontally near the rigid lower surface. The nonlinear effects are studied by inspecting individual terms. In the heating case, the advection of the zonal wind tends to accelerate the air near the heating center, while the temperature advection acts as an additional weak heat sink to the system. Thus the overall nonlinear effect in the heating case is to strengthen the disturbance. In addition, the nonlinear effects act to contract the disturbance into a narrower area. In the cooling case, both the advection of the zonal wind and temperature are dominated by the vertical advection terms. The advection of the zonal wind tends to accelerate the air on the left side of the heating center toward the heating center. Thus it tends to weaken the disturbance. Similarly, the disturbance is weakened by the nonlinear temperature advection which acts as an additional strong heat source. In other words, the overall nonlinear effect in the cooling case is to weaken the disturbance. Besides, both nonlinear advections are spread out to a wider area, which are responsible for the wider disturbance. The nonlinear effects for cases with heating centered at a higher latitude are similar.

In considering the effects of Atlantic SSTA on wind patterns in the Sahel and northeastern Brazil, the SSTA is represented by low-level diabatic forcing in the numerical model. With a coupled warm SSTA in the South Atlantic and cold SSTA in the North Atlantic, it tends to produce an offshore flow and weak downward motion in the Sahel. This may reduce the chance of convection and possibly a negative rainfall anomaly. In northeastern Brazil, there exists an upward motion and an offshore flow. When the SSTA pattern is reversed, the onshore flow and upward motion produced in the western Sahel which may trigger more convection and possibly produce a positive rainfall anomaly. In the eastern part of northeast Brazil, although the onshore flow is very strong, the downward motion tends to suppress convection and could reduce the amount of rainfall there.

The readers should keep in mind that a number of assumptions have been made in the present model and many physical processes are not taken into consideration, for example, latent heating, boundary layer physics, and air-sea interaction. This work will be extended to include those effects and a more realistic basic state flow in the future. However, the present work does provide some physical insight in the flow response in a simple idealized atmosphere to low-level heating. These results could be beneficial in interpreting and supplementing the GCM results.

Acknowledgments. The author would also like to thank R. P. Weglarz for his help in model development, editing the manuscripts and useful discussions. This research is supported by NOAA under the Grant NA26GP0103-01 and NA56GP0390. The computations were performed on the supercomputer at North Carolina Supercomputing Center and the workstations acquired through the IBM FOAM^{V} equipment grant.

References

Asselin, R., Frequency filter for time integrations, *Mon. Weather Rev., 100*, 487-490, 1972.

Bjerknes, J., A possible response of the atmospheric Hadley circulation to equatorial anomalies of ocean temperature, *Tellus, 18*, 820-829, 1966.

Chervin, R. M., and S. H. Schneider, On determining the statistical significance of climate experiments with general circulation models, *J. Atmos. Sci., 33*, 405-412, 1976.

Druyan, L., GCM studies of the African summer monsoon, *Clim. Dyn., 2*, 117-126, 1987.

Druyan, L., Advances in the study of Sub-Saharan drought, *Int. J. Clim., 9*, 77-90, 1989.

Egger, J., On the linear theory of the atmospheric response to sea surface temperature anomalies, *J. Atmos. Sci., 34*, 603-614, 1977.

Folland, C., T. Palmer, and D. Parker, Sahel rainfall and worldwide sea temperatures, 1901-85, *Nature, 320*, 602-607, 1986.

Gill, A. E., Some simple solutions for heat-induced tropical circulation, *Q. J. R. Meteorol. Soc., 106*, 447-462, 1980.

Gill, A. E., and P. J. Phlips, Nonlinear effects on heat-induced circulations of the tropical atmosphere, *Q. J. R. Meteorol. Soc., 112*, 69-91, 1986.

Hastenrath, S., On modes of tropical circulation and climate anomalies, *J. Atmos. Sci., 35*, 2222-2231, 1978.

Hastenrath, S., Interannual variability and annual cycle: Mechanisms of circulation and climate in the tropical Atlantic sector, *Mon. Weather. Rev., 112*, 1097-1107, 1984.

Hastenrath, S., and L. Heller, Dynamics of climate hazards in Northeast Brazil, *Q. J. R. Meteorol. Soc., 103*, 77-92, 1977.

Houghton, D. D., J. E. Kutzbach, M. McClintock, and D. Suchman, Response of a general circulation model to a sea temperature perturbation, *J. Atmos. Sci., 31*, 857-868, 1974.

Klemp, J. B., and D. R. Durran, An upper boundary condition permitting internal gravity wave radiation in numerical mesoscale model, *Mon. Weather Rev., 111*, 430-444, 1983.

Kundu, P. K., *Fluid Mechanics*, 638 pp, Academic, San Diego, Calif., 1990.

Lamb, P. J., Large-scale tropical Atlantic surface circulation patterns associated with sub-Saharan weather anomalies, *Tellus, 30*, 240-251, 1978.

Lin, C. A., and R. E. Stewart, Diabatically forced mesoscale circulations in the atmosphere, *Adv. Geophys., 33*, 267-305, 1991.

Lin, Y.-L., Airflow over mesoscale heat source, I, Responses in a uniform flow, *NSC, 18*, 1-32, 1994a.

Lin, Y.-L., Airflow over mesoscale heat source, II, Responses in a shear flow, *NSC, 18*, 119-150, 1994b.

Lin, Y.-L., T.-A. Wang, and R. P. Weglarz, Interaction between gravity waves and cold air outflows in a stably stratified uniform flow, *J. Atmos. Sci., 50*, 3790-3816, 1993.

Lindzen, R. S., and S. Nigam, On the role of sea surface temperature gradients in forcing low-level winds and convergence in the tropics, *J. Atmos. Sci., 44*, 2418-2436, 1987.

Liu, Q., and C. J. E. Schurmans, The linearity of the atmospheric response to tropical Pacific anomalous forcing, *J. Clim., 6*, 862-875.1993.

Lough, J., Tropical Atlantic sea surface temperatures and rainfall variations in Subsaharan Africa, *Mon. Weather Rev., 114*, 561-570, 1986.

Markham, C. G., and D. R. McLain, Sea surface temperature related to rain in Ceara, northeast Brazil, *Nature, 265*, 320-323, 1977.

Matsuno, T., Quasi-geostrophic motions in the equatorial area, *J. Meteorol. Soc. Jpn., 44*, 25-43, 1966.

Moura, A. D., and J. Shukla, On the dynamics of droughts in northeast Brazil: Observations, theory and numerical experiments with a general circulation model, *J. Atmos. Sci., 38*, 2653-2675, 1981.

Nicholson, S., Sub-Saharan rainfall 1981-84, *J. Clim. Appl. Meteorol., 24*, 1388-1391, 1985.

Nicholson, S., J. Y. Kim, and J. Hoopingarner, ATLAS of African rainfall and its interannual variability, Ph.D. dissertation, 237 pp., Dept. of Meteorol., Florida State Univ., Tallahassee, Florida, 1988.

Orlanski, I., A simple boundary condition for unbounded hyperbolic flow, *J. Comput. Phys., 21*, 251-269, 1976.

Palmer, T. N., Influence of the Atlantic, Pacific, and Indian oceans on Sahel rainfall, *Nature, 322*, 251-253, 1986.

Palmer, T. N., and D. A. Mansfield, A study of wintertime circulation anomalies during past El Nino events using a high resolution general circulation model, I, Influence of model climatology, *Q. J. R. Meteorol. Soc., 112*, 613-638, 1986.

Parker, D., C. Folland, and M. Ward, Sea-surface temperature anomaly patterns and prediction of seasonal rainfall in the Sahel region of Africa, in *Recent Climatic Change, 15*, Belhaven, London, 1988.

Phlips, P. J., and A. E. Gill, An analytical model of the heat-induced tropical circulation in the presence of a mean wind, *Q. J. R. Meteorol. Soc., 113*, 213-236, 1987.

Rao, V. B., M. C. De Lima, S. H. Franchito, and J. Servain, On the role of the coastal wind in the interannual variations of rainfall over eastern northeast Brazil, *TOGA notes, 9*, pp. 12-16, Trop. Ocean-Global Atmos., 1992.

Ratisbona, C. R., The climate of Brazil in *Climates of Central and South America*, vol. 12, *World Survey of Climatology*, edited by W. Schwerdtfeger and H. E. Landsberg, pp. 219-293, Elsevier, New York, 1976.

Rowntree, P. R., The influence of the tropical east Pacific Ocean temperature on the atmosphere, *Q. J. R. Meteorol. Soc.*, *98*, 290-321, 1972.

Schneider, E. K., and R. S. Lindzen, Axially symmetric steady-state models of the basic state for instability and climate studies, I, Linearized calculations, *J. Atmos. Sci.*, *34*, 263-279, 1977.

Semazzi, H. F. M., Y. C. Sud, and V. Mehta, An investigation of the relationship between sub-Saharan rainfall and global sea-surface temperatures, *Atmos. Ocean*, *26*, 118-138, 1988.

Shapiro, R., Smoothing, filtering, and boundary effects, *Rev. Geophys.*, *8*, 359-387, 1970.

Shukla, J., and J. M. Wallace, Numerical simulation of the atmospheric response to equatorial Pacific sea surface temperature anomalies, *J. Atmos. Sci.*, *40*, 1613-1630, 1983.

Silva Dias, P. L., W. H. Schubert, and M. DeMaria, Large-scale response of the tropical atmosphere to transient convection, *J. Atmos. Sci.*, *40*, 2689-2707, 1983.

Smith, R. B., and Y.-L. Lin, The addition of heat to a stratified airstream with application to the dynamics of orographic rain, *Q. J. R. Meteorol. Soc.*, *108*, 353-378, 1982.

Spar, J., Some effects of surface anomalies in a global general circulation model, *Mon. Weather Rev.*, *101*, 91-100, 1973.

Stevens, D. E., and R. S. Lindzen, Tropical wave-CISK with a moisture budget and cumulus friction, *J. Atmos. Sci.*, *35*, 940-961, 1978.

Webster, P. J., Response of the tropical atmosphere to local steady forcing, *Mon. Weather Rev.*, *100*, 518-541, 1972.

Webster, P. J., Mechanisms determining the atmospheric response to sea surface temperature anomalies, *J. Atmos. Sci.*, *38*, 554-571, 1981.

Weglarz, R. P., Three-dimensional geostrophic adjustment of rotating homogeneous and continuously stratified atmospheres with application to the dynamics of midlatitude jet streaks, Ph.D. thesis, 414 pp., North Carolina State Univ., Raleigh, 1994.

G. S. Janowitz, Y.-L. Lin, H.F.M. Semazzi[1], and T.-A. Wang, North Carolina State University, Department of Marine, Earth and Atmospheric Sciences, Box 8208, Raleigh, NC 27695-8208. (e-mail: janowitz@ncsu.edu; yl_lin@ncsu.edu; fred_semazzi@ncsu.edu; tawang@meavax.nrrc.ncsu.edu)

(Received January 25, 1995; revised August 16, 1995; accepted November 22, 1995.)